Observational Study of Activities on the Solar Surface

Kencihi OTSUJI

Department of Astronomy, Kyoto University, Sakyo-ku, Kyoto 606-8502

otsuji@kwasan.kyoto-u.ac.jp

2008.02.04

Acknowledgement

Abstract

In this thesis I present my studies about active phenomena observed on the solar surface. The main subjects of the study are magnetic flux emergence and filament eruption. This thesis consists of three parts.

The part one is about an emerging flux region observed at Hida observatory. With a method called "cloud model", I obtained the Doppler velocity map of rising magnetic flux. The evolution of magnetic field strength is also studied. And discussions are given on the effect of preexistent magnetic field on the dynamics of flux emergence.

In the part two, I summarize my paper published in 2007 November 30, in PASJ. The paper contains the initial result of Hinode, a highly sophisticated observational satellite. With the highest resolution of solar optical telescope aboard Hinode, I studied the evolution of a small emerging flux region, mainly from the morphological point of view. Discussions are given by referencing to the theoretical simulation works.

In the part three, I applied the same method as the part one to a filament eruption observed at Hida observatory. The Doppler velocity of erupting filament is combined with the tangential velocity of the apparent motion to obtain three dimensional velocity distribution. I estimated the mass distribution of the filament to obtain the kinetic energy (rotational and translational energy) of the eruptive filament. I believe that the detailed quantitative estimate of erupting filament energy provide basic data for clearing the driving mechanism of the eruption.

Introduction

Solar surface is full of active phenomena. Among them, magnetic flux emergence from below the photosphere plays a very important role in solar activities. Surge (Roy 1973) and Ellerman bomb (Ellerman 1917) are observed at the region where emerging flux are appearing (Kurokawa 1988; Pariat et al. 2004). These phenomena are now well explained by magneto-hydrodynamic simulations as the result of reconnection between the emerging flux tube and preexisting coronal magnetic field (Yokoyama and Shibata 1996, Isobe et al. 2007b). Also solar flares are thought to be triggered by emerging flux (Tur and Priest 1978). Shibata et al. (1992) carried out two dimensional magneto-hydrodynamic simulation of flares triggered by emerging flux.

The mechanism of flux emergence has been investigated and simulated for a long time. Zwaan (1978) explained that magnetic flux tube is concentrated by the differential rotation of the Sun into the toroidal bundle, then the bundle begins rising by Parker instability (Parker 1966). Shibata et al. (1989) carried out a magneto-hydrodynamic simulation and suggested that an emerging flux makes a self similar evolution. But the observational investigation of emerging flux regions is not so enough, especially for the initial phase of them, because it is difficult to predict where a new emerging flux region appears. To solve this problem, full disk observation is required. Solar magnetic activity research telescope in Hida observatory was installed to work for this requirement. Its T1 telescope can observe full disk image of the Sun in multi-wavelengths near Hα line. Using the T1 telescope we succeeded in getting initial evolution of an emerging flux region. We investigated the time series observational data and obtained the temporal variation of the Doppler velocity map of the emerging flux region. The relation among the evolution of geometrical configuration, rise velocity and magnetic field strength is discussed in part one.

Wide field of view is an advantage of ground-based observation, but it is generally affected by the atmospheric fluctuation. Meanwhile spacecraft observation is free from the seeing problem, though it is difficult to observe with large field of view because of the less telemetry power. Hinode satellite was lunched on 2006 September 23, for the purpose of unveiling detailed particulars of solar activities with its very high spatial resolution. Hinode has already made lots of discoveries. For example, "the ubiquitous jet" is found on the solar surface (Shibata et al. 2007), which made us to change the image of the Sun. Furthermore, the microscopic feature inside a sunspot are investigated by Kitai et al. (2007). As presented in these studies, improvement in the spatial resolution opens the door to the new discoveries. In part two, we investigated the nature of emerging flux in the quite initial phase of its appearance. From detailed analysis, we conclude that the emerging flux region expands along its axis of magnetic flux rapidly ($\sim$ 4km s^{-1}) in the first several minutes, then decelerates expansion to about 1km s^{-1}. The lifetime of an arch filament is about 12 minutes. The lateral expansion of an arch filament is quantitatively measured for the first time to be 3.8km s^{-1}in initial phase of emergence.

Several active phenomena on the solar surface are accompanied by emerging flux. Recently emerging flux is considered as a trigger of flare (Shibata et al. 1992; Isobe et al. 2007a). And when flare occurs, a filament eruption occasionally takes place (Kurokawa

et al. 1987). The erupted filament into interplanetary space is involved in a coronal mass ejection and sometimes strikes the Earth and induces strong magnetic storm (Wright and McNamara 1983). In part three we applied the method introduced in part one to a rotational eruptive filament off the solar limb. The observation was done with solar magnetic activity research telescope at Hida observatory. We estimated the kinetic energy of the eruptive filament from the distributions of three dimensional velocity and mass density. This study determines the distribution ratio of the energy released by magnetic reconnection into the radiation and kinetic energy. Analyzing of energy distribution will be helpful to investigate the mechanism of filament eruption, including flare.

References

Ellerman, E. 1917, ApJ, 26, 298

Isobe, H., Tripathi, D., Archontis, V. 2007, ApJ, 657L, 531

Isobe, H., Tripathi, D., Asai, A., Jain, R. 2007, Sol. Phys., 246, 89l

Kitai, R. et al. 2007, PASJ, 59, 585

Kurokawa, H., Hanaoka, Y., Shibata, K., & Uchida, Y. 1987, Sol. Phys., 108, 251

Kurokawa, H. 1988, Vistas Astron., 31, 67

Pariat, E., Aulanier, G., Schmieder, B., Georgoulis, M. K., Rust, D. M., & Bernasconi, P. N. 2004, ApJ, 614, 1099

Perker, E. N. 1966, ApJ, 145, 491

Roy, J. R. 1973 Sol. Phys., 32, 139

Shibata, K., Tajima, T., Steinolfson, R. S., & Matsumoto, R. 1989, ApJ, 345, 584

Shibata, K., Nozawa, Satoshi, & Matsumoto, R. 1992, PASJ, 44, 265

Shibata, K. et al. 2007, Science, 318, 1591

Tur, Y. J., & Priest, E. R. 1978, Sol. Phys., 58, 181

Wright, C. S., & McNamara, L. F. 1983, Sol. Phys., 87, 401

Yokoyama, T., & Shibata, K. 1996, PASJ, 48, 353

Zwaan, C. 1978, Sol. Phys., 60, 213

Contents

Part I
Observational Study of Emerging Flux Regions Using Solar Magnetic Activity Research Telescope

Abstract

We observed an emerging flux region with solar magnetic activity research telescope (SMART) at Hida observatory. The observation has been done since 18 until 21 Aug 2005. By using SMART, we obtained images of the emerging flux region taken with 5 wavelength near the Hα. Applying the observation data to the Beckers' cloud model, we derived physical parameter of the emerging flux region. From the distribution and time evolution of Doppler velocity, we conclude that The range of rise velocity is -1.8 km s^{-1} $\sim$ -20.1 km s^{-1}. The lifetime of arch filaments is 11-35 minutes but there are some arch filaments seems appear to have long lifetime. From MDI magnetogram data, the evolution of the distance between two polarities are obtained. The orientation angle of bipole axis shows the 60 degrees rotation during the emergence.

1 Introduction

An emerging flux region (EFR) is the early phase of an active region (AR). In an EFR, magnetic flux loops lying underneath the photosphere emerges into the chromosphere and the corona (Bruzek 1969; Zirin 1972).

Zwaan (1978) concluded the mechanism of magnetic loop emergence as follows; (i) solar poloidal field is concentrated to about 500 G in toroidal bundles by differential rotation, (ii) in the deep convection zone the flux bundles rise by the Parker instability (Parker 1966; Parker 1969), (iii) the top of the flux tubes surface to the photosphere and radiative cooling reduce the temperature of the flux tubes, then the footpoints of flux tubes are rapidly concentrated to values up to 1800 G by convective collapse (Parker 1978; Spruit 1979). Once the magnetic loop reached to the solar surface, they expand toward the corona by the magnetic pressure inside the flux tubes (Shibata et al. 1989a; Shibata et al. 1989b).

With white light, EFR shows bright points or pores which are footpoints of magnetic flux loops and between them dark lanes are observed (Miller 1960; Loughhead and Bray 1961; Brants and Steenbeek 1985). Using Hα line filtergram, several dark loops connecting both polarity of the EFR are observed at the height of the chromosphere. These loops are named "arch filament systems (AFS)" by Bruzek (1967) and each dark loops (arch filament) in an AFS are thought to trace the magnetic field around the EFR.

The dynamic characteristics and the physical parameter of AFS have been studied by Bruzek (1967), Roberts (1970), Frazier (1972), Chou and Zirin (1988) and so on. The lifetime of an arch filament is 10-30 minutes. Individual arch filaments in an AFS are about 1000-3000 km. The entire AFS reaches an extent of 20000-40000 km.

Arch filaments rise at a speed of 5-20 km s^{-1} at the top of the loops. Near the both footpoints downflow motion is observed to be 35-50 km s^{-1} (Bruzek 1969; Roberts 1970; Zwaan 1985; Chou and Zirin 1988).

As magnetic flux loops emerge, two magnetic polarities representing the footpoints of magnetic flux loops separate each other and the EFR expands. Strous et al. (1996) measured the separation speed of both polarities of an EFR to be less than 1 km s^{-1}. Harvey and Martin (1973) observed ephemeral active regions and suggested that in the first few minutes of the emergence the separation rate is about 5 km s^{-1} and decreases to 0.7-1.3 km s^{-1}. Recently Otsuji et al. (2007) observed a small scale EFR with Hinode and showed that two footpoints separate each other at a speed of 4.2 km s^{-1} during the initial phase of evolution, and 10 minutes later the speed decreases to about 1 km s^{-1}.

The emerged magnetic flux often causes reconnection with the magnetic flux preexisting in the corona and responsible for flares (Heyvaerts et al. 1977; Shibata et al. 1992a; Shibata et al. 1992b; Shibata 1998; Shimizu et al. 2002).

Shibata et al. (1989b) performed two-dimensional magneto-hydrodynamic (MHD) simulations of emerging flux for the first time, and well explained the velocity field of observed EFRs. Subsequently, three-dimensional simulation of EFR were done by Matsumoto and Shibata (1992).

In this paper we applied Beckers' cloud model (Beckers 1964) to EFR observed by solar magnetic activity research telescope (SMART) at Hida observatory. Although there is also past study applying the cloud model to EFR (Tsiropoula et al. 1992), but their study is based on just 15 minutes observation data, so long-term evolution of ascending velocity of EFR hasn't be investigated. This time we observed an EFR from its time of birth and followed its evolution for three days.

2   Observation

2.1   Hα Observation

The observation was done with using SMART at Hida observatory. SMART has 4 telescopes (T1-T4), and in this study we used the data obtained by T1 telescope. SMART T1 telescope's purpose is monitoring constantly the solar surface. So at any time T1 telescope is observing solar activities, except when it is cloudy day or night.

T1 telescope observes solar surface with the wavelength of Hα line center. The tunable range of Lyot filter (Lyot 1944) is 6562.808±2.0Å. T1 telescope has 20 cm aperture and covers full-disk of solar surface. The total field of view (FOV) is 2300″ × 2300″. The passband of Lyot filter is 0.25Å (FWHM). On the focal plane there is a 4096 × 4096 pixels CCD and pixel size is 0″.58/pixel (Ishii et al. 2004). Spatial resolution and time resolution of the observation are ∼ 1″ and 40 seconds for each wavelength, respectively. Wavelengths of observation are Hα line center, Hα±0.5Å and Hα±0.8Å. It takes about 30 seconds to obtain one wavelengths set.

2.2 Magnetogram Observation

The magnetic field configuration is important for discussing EFR. In this study we used the magnetogram data from Michelson Doppler Imager (MDI) of SOHO. MDI supplies full-disk magnetogram with FOV of $2000'' \times 2000''$. The CCD size is 1024×1024 pixels and the pixel size is $1''.99$/pixel. Every 1 minute the magnetogram images is taken.

Hagenaar (2001) mentioned the noise level of MDI magnetogram to be 14 G. So in this study the signals below 14 G are treated as noises.

2.3 Identification of EFR

We identified EFRs by comparing the observation data of SMART T1 telescope and SOHO MDI data. Figure 1 and 2 show the daily solar images from 2005 August 17 (Day 0) to 2005 August 20 (Day 3). On Day 0 Hα image, there are two ARs on the southern hemisphere of the Sun. The east AR is NOAA 10797 and the west AR is NOAA 10798. In the previous rotation phase, (2005 July 21), there is no AR on solar surface. In the picture of Day 2, we can recognize a small brightening at east region of NOAA 10798 in the Hα image, though it is difficult to see any signature of EFR in the magnetogram. Day 3 pictures show more clearly the EFR. In the magnetogram there appear a pair of opposite polarities at the same location as the Hα brightening. On Day 4, two sunspots are formed in the Hα image. In the magnetogram the footpoint polarities of the EFR seem to be expanding. Note that the magnetic orientation of the EFR is not following the Hale's low (Hale et al. 1919).

In this study we investigated this EFR from the point of morphology, evolution of rise velocity and magnetic field strength.

3 Data Reduction

3.1 Calibration for Hα Images

The obtained Hα images are calibrated by dark subtraction and flat fielding. Then the Sun center is detected by limb fitting and solar p angle is corrected.

Next, from all observation data, we selected appropriate data sets which are unaffected by clouds. Images in Hα line center, ± 0.5 Å and ± 0.8 Å observed consecutively without cloud intervention are selected as a dataset for Doppler analysis. In table 1, the first (left) column shows the observation days. The second and third columns present the observational dates of Hα center images in the initial and final set of each day, respectively. The final column shows the number of data set of each day.

The number of data set of the first day is fairly less than that of the third day, due to the frequent passage of clouds in the first day.

In this paper we obtained the physical parameters of AFS in the EFR by using Beckers' cloud model (1). We calculated the observed contrast $C'(\Delta\lambda)$ as follows. In each data set, the EFR is clipped by the FOV of the $150''\times150''$. The background images are obtained by smoothing the quiet region in the clipped data for each wavelength. Then the background images are subtracted from the corresponding wavelength images. The subtracted images
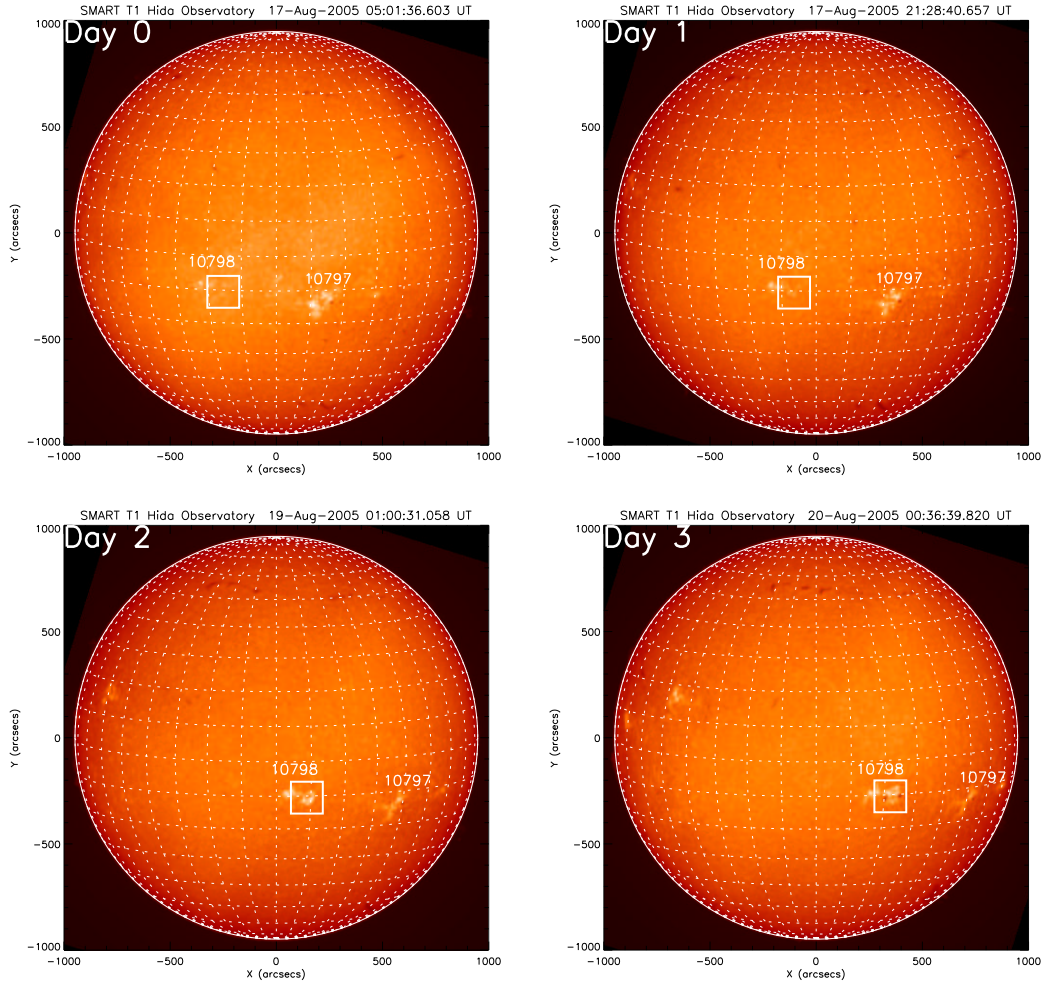
Figure 1: Solar images observed by SMART T1 telescope with Hα line center. Upper left, upper right, lower left and lower right panel show the pictures of day 0 (before the EFR appearance), day 1, day 2 and day 3, respectively. In each panel, white box shows the position of new EFR. The preexisting ARs in the south-east and south-west parts of day 0 solar image are NOAA 10797 and 10798, respectively.

Table 1: Selected data sets on each days

Day #	Initial set	Final set	# of data sets
Day 1	2005 August 17 20:44:17 UT	2005 August 18 07:52:23 UT	99
Day 2	19 01:01:09 UT	19 08:13:00 UT	151
Day 3	19 21:31:48 UT	20 07:39:10 UT	395

are divided by the background, then we obtain the contrast images. The contrast set of the same point on each wavelength image are picked up and applied to Beckers' cloud model. Observed contrast sets $\left(C'(-0.8\text{Å}), C'(-0.5\text{Å}), C'(\pm0.0\text{Å}), C'(+0.5\text{Å}), C'(+0.8\text{Å})\right)$ are fitted by the theoretical contrasts $C(\Delta\lambda)$ reconstructed from given physical parameters S, τ_0, $\Delta\lambda_\mathrm{D}$ and $\Delta\lambda_\mathrm{D}$. To calculate the theoretical contrast $C(\Delta\lambda)$, the reference Hα profile is used Kurucz (2005). To fit the theoretical contrast $C(\Delta\lambda)$ to the observed
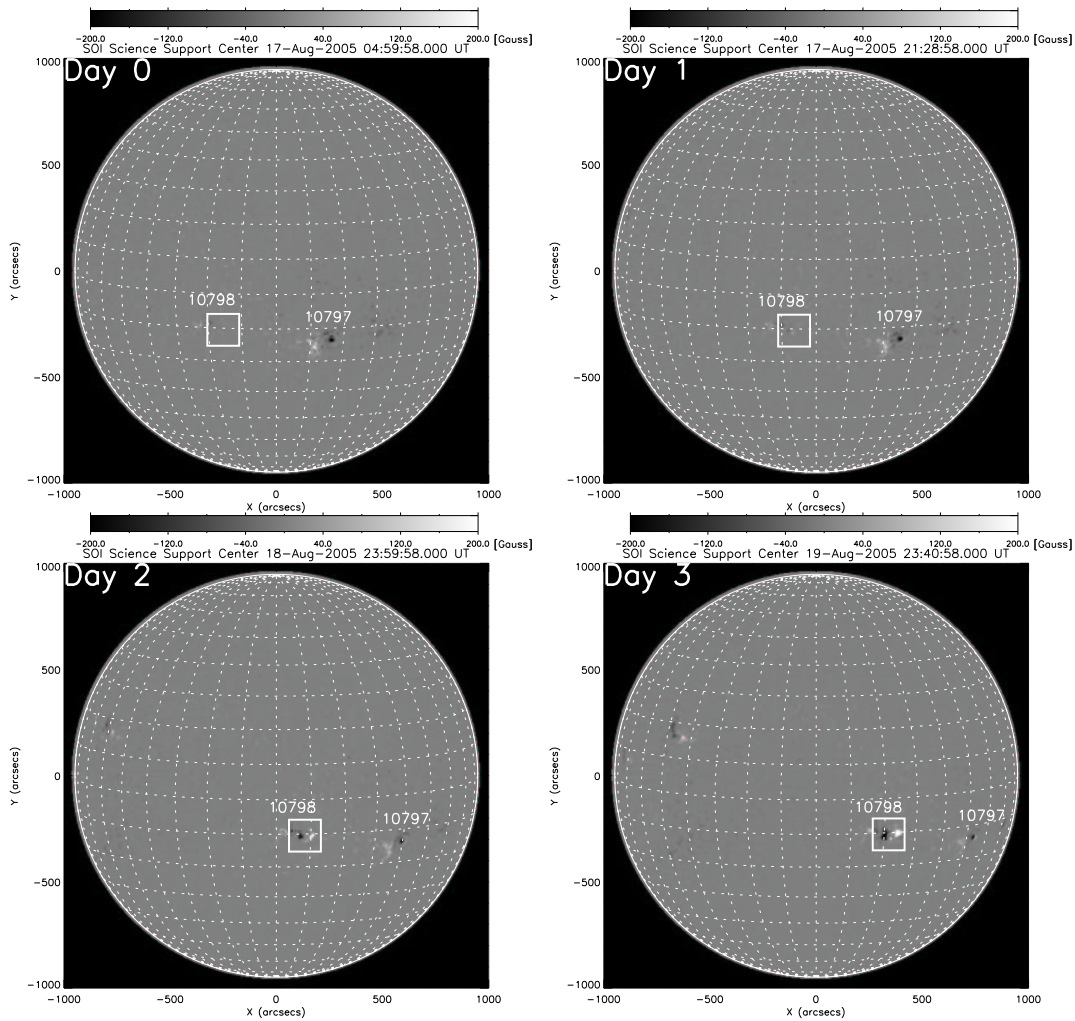
11

Figure 2: Solar images observed by SOHO MDI T1 magnetogram. Upper left, upper right, lower left and lower right panel show the pictures of day 0 (before the EFR appearance), day 1, day 2 and day 3, respectively. In each panel, white box shows the position of new EFR. Gray scale covers the range of $-200 \sim +200$ G.

contrast $C'(\Delta\lambda)$, an iteration method were carried out. An suitable initial parameters are substituted to the cloud model and the theoretical contrast $C(\Delta\lambda)$ is calculated. Then the difference between $C(\Delta\lambda)$ and $C'(\Delta\lambda)$ is obtained, and according to that the input parameters are revised using "hybrid method" (Powell 1970). We iterated this fitting for all pixels in the data set and obtained two dimensional Doppler velocity map of the EFR.

3.2 Calibration for Magnetogram Images

One pixel of MDI magnetogram covers the area of $S_\perp \approx 2'' \times 2''$. When α is defined as the center angle between the disk center and a pixel which coordinate is (x, y) on the disk, α is described as

$$\alpha = \sin^{-1}\left(\frac{\sqrt{x^2 + y^2}}{R}\right), \tag{1}$$

where (x, y) is measured from the disk center and R is the solar radius in pixel. Using α, the corresponding area on the solar surface to the pixel (x, y) is

$$S(\alpha) = \frac{S_\perp}{\cos(\alpha)}. \tag{2}$$

We consider all magnetic flux to be perpendicularly set on the solar surface (Murray 1992). If so, observed magnetic field strength $B(\alpha)$ is a projection component onto the line-of-sight direction:

$$B(\alpha) = B_\perp \cos(\alpha), \tag{3}$$

where $B_\perp$ is the real magnetic field strength. From equation (3), $B_\perp$ is described as

$$B_\perp = \frac{B(\alpha)}{\cos(\alpha)}. \tag{4}$$

In the paper of Hagenaar (2001), only the region of $\alpha \leq 60°$ is studied, because $1/\cos(\alpha)$ in equation (2) and (4) reaches infinity as α approximates 90°. In this study, the position of EFR is near the disk center through the period, so these corrections are appropriate.

4 Result

4.1 Morphological Evolution of the EFR

4.1.1 Day 0

Figure 3 shows the quiet solar surface before the appearance of the EFR. The observation time is 05:01:29 UT on 2005 August 17 (Day 0) for Hα line center image. There are dark blobs appeared in the wing images, which are called "dark mottles" (Macris 1957) and thought as spicules on solar disk (Banos and Macris 1970). In Hα line center image we can see some plages that correspond to magnetic concentrations in the magnetogram. The negative magnetic concentration shown by n in magnetogram is preceding polarities of NOAA 10978.

4.1.2 Day 1

The new EFR appeared on the August 17 (morning on 18 in JST). When the observation started the EFR has began to emerge already.

In figure 4 there is a small AR newly emerging. The observation time is 21:31 UT on August 17. In magnetogram image, new bipole (N_1 and P_1) are shown. The distance between two magnetic polarity is about $20''$. Hα line center image shows two bright plages corresponding to the both footpoints of the EFR. There is a filament (F_1) laying at north of N_1. Between two footpoints there are three arch filaments (1, 2, and 3). The magnetic field at the footpoints are about 80 G.

Figure 5a, 5b and 5c are a series of images following the evolution of arch filaments. The interval between each figure is about 20 minutes.
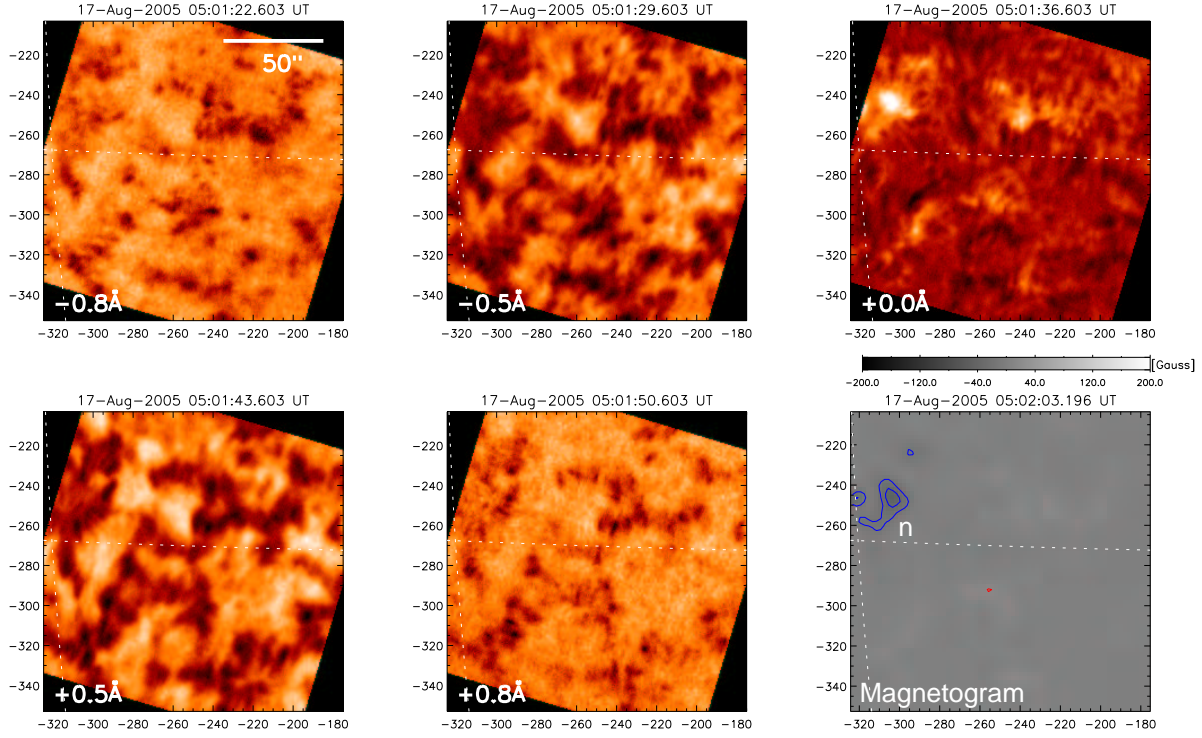
Figure 3: The images of solar surface observed by Hα and magnetogram at 05:01 UT on 17 August (Day 0), before the EFR's appearance. The FOV is indicated in figure 1 and 2 by white box. Left, middle and right panels in upper row show Hα−0.8Å, −0.5Å and line center images, and those in lower row show Hα+0.5Å, +0.8Å and MDI magnetogram, respectively. The interval of contours in the magnetogram is 20 G (blue for negative and red for positive). An preexisting magnetic concentration of NOAA 10978 is represented by n in the magnetogram.

After 9 hours from figure 4 (06:37 UT on August 18), the EFR spread out to east-west direction (Figure 5a). The distance between P_1 and N_1 is 30″, so the average expansion rate for this period is 1.1″ per hour (0.22 km s^{-1}). In the Hα line center image, we can see bright plages. Three arch filaments (4, 5 and 6) connect the plages. The arch filaments also appear in the Hα wing images. A filament (F_2) is formed at the south-east part of the EFR, while F_1 disappeared. The orientation of the axis of bipole is smaller than that in figure 4.

Figure 5b shows about 20 minutes later of figure 5a (06:58 UT). The Arch filament 4 and 6 become transparent for Hα. But arch filament 5 is still seen in all wavelengths. In Hα+0.8Å image there is a bright point (B_1) between the footpoints of the arch filament 5. This bright point is not observed in the other images. It is clearly shown that at the footpoints there exist strong downflow shown in Hα+0.5Å and +0.8Å images. In the blue wing images, we can see the upward motion near the apex of the arch filament.

Figure 5c shows the images of the EFR another 20 minutes later (07:17 UT). While the arch filament 5 faded out, a new arch filament is formed (7 in Hα line center image). A surge (S_1) is observed at south of the EFR in the blue wing images.
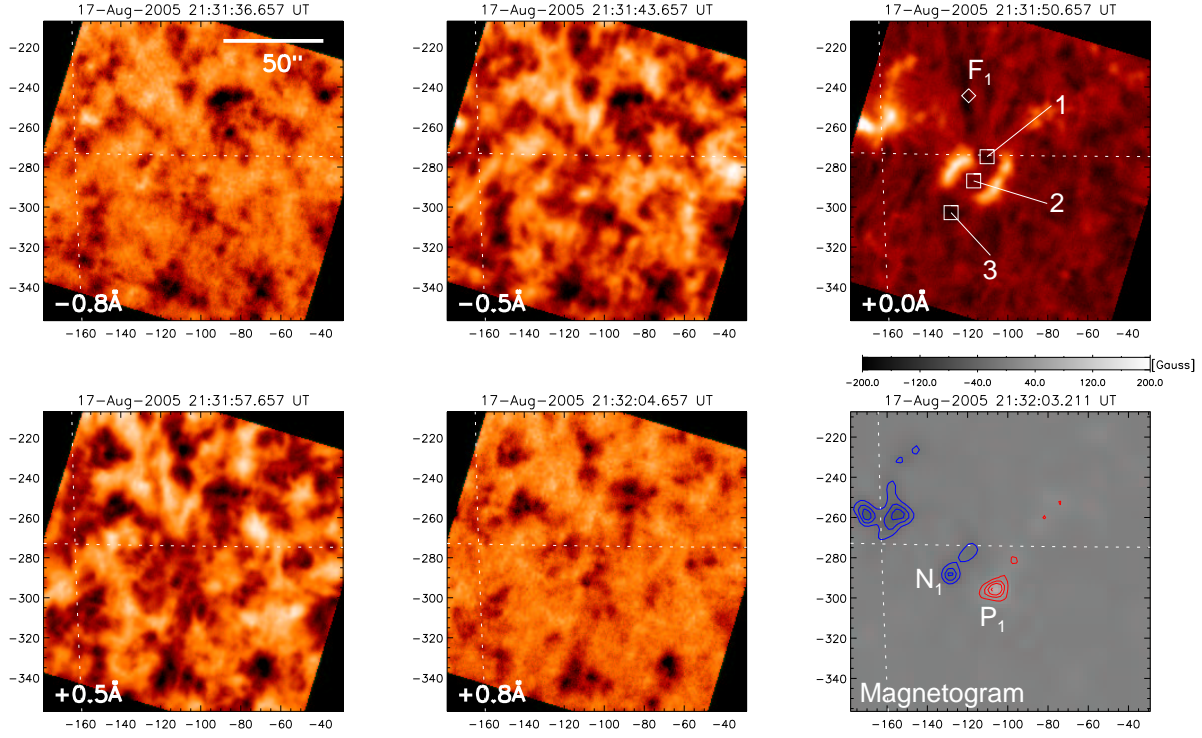
Figure 4: The images of the EFR on its initial stage of emergence. The observation time is 21:31 UT on August 17 (Day 1). The arrangement of images is same as figure 3. In Hα line center image there are three arch filaments indicated by 1, 2 and 3. The magnetogram image shows the new bipole (N_1 and P_1). There is a filament (F_1) lying on north of N_1.

4.1.3 Day 2

Figure 6-9 represent the evolution of EFR on Day 2 (August 19 in JST). The EFR became enlarged and the sunspot are formed. The size of each arch filament is longer than that of Day 1. The axis of the bipole and latitude lines are almost parallel.

In figure 6 there is the developed EFR observed at 23:43 UT on 18 August. Three arch filaments are prominent (shown in Hα line center image as 8, 9 and 10). In Hα images, two sunspots and several small pores are formed at the footpoints of the arch filaments. In the Hα±0.8Å images there are several bright (B_2, B_3 and B_4). The magnetic field at the footpoints are about 300 G. The distance between two main polarity (N_1 and P_1) is about 60″.

One hour later, there are three arch filaments (11, 12 and 13) in figure 7. The observation time is 00:55 UT on 19. We can see some bright (B_5, B_6 and B_7). Among them, B_5 locates on the east footpoint of arch filament 12. Arch filament 11 is visible in Hα wing images, but the others are not so prominent. The plages are appeared brighter in Hα−0.5Å image than those in Hα+0.5Å.

Figure 8 shows the EFR observed at 02:51 UT. 4 arch are lying between the footpoints (14, 15, 16 and 17). Arch filament 14 and 17 are prominent in Hα wing images. Through the figure 6 to 8, the appearance position of bright points is almost the same place.

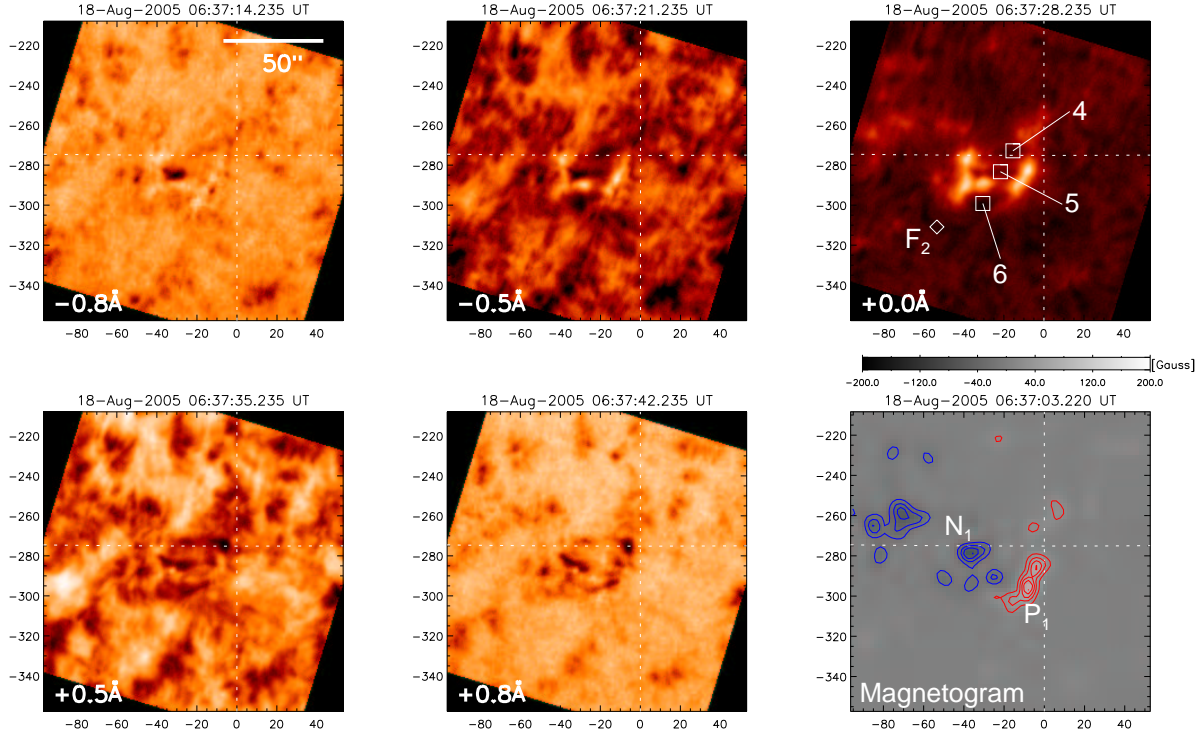Figure 9 is obtained at 04:48 UT. There are 5 arch filaments. The arch filaments

15

Figure 5a: The EFR observed at 06:37 UT. There are three arch filaments jointing the two plages in Hα line center and wing images.

located outer side of EFR show strong absorption in Hα wing images (arch filament 18, 21 and 22). The inner arch filament (19 and 22) seems to be quiescent. The pores observed in figure 6 merged together and formed new sunspots (N_2 and P_2) at south of each main spot (N_1 and P_1). In magnetogram, The pattern of the magnetic field is seen to be arranged alternately between both main spots.

4.1.4   Day 3

On Day 3 (August 20 in JST), The EFR developed larger (figure 10, 11 and 12). Two main sunspots formed penumbrae around them. The field strength at the footpoints is $300 \sim 400$ G. The distance between two main polarity (N_1 and P_1) is about $60''$ on the image, but due to the projection effect, the actual distance is somewhat larger.

Figure 10 is observed at 23:54 UT on August 19. There are 6 arch filaments and the outer filaments show strong absorption in the Hα wing images. N_2 and P_2 sunspots observed in figure 9 merged with the main spots (N_1 and P_1). An satellite spot of positive polarity (P_3 and P_4) are formed between N_1 and P_1. Arch filaments 25 connects with N_1 and P_3. P_4 spot is the footpoint of arch filament 27 and 28.

Figure 11 shows the EFR at 05:18 UT on August 20. There are many satellite spots between the main spots. 6 arch filaments are observable in Hα center image. Arch filament 29 connects N_3 and P_1. At the footpoint of arch filament 29, a bright point B_{11} exists. The position of B_{11} corresponds to the contact surface of N_3 and P_5. A surge
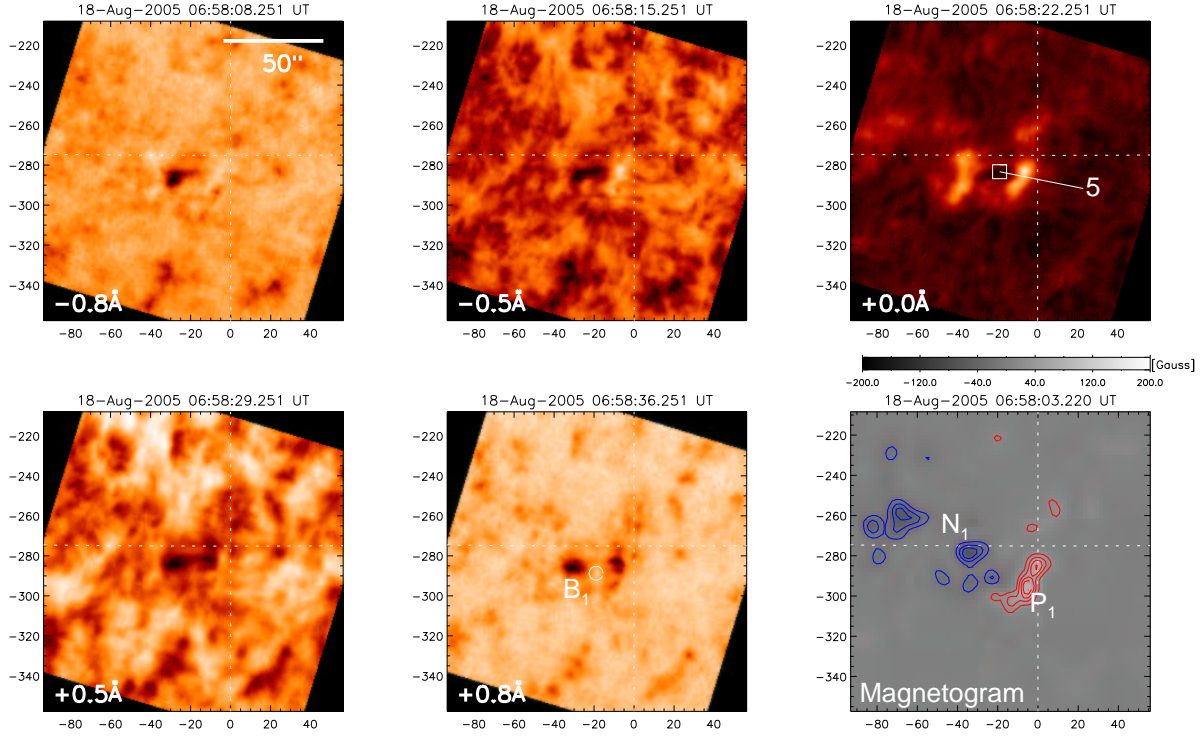
Figure 5b: The EFR observed at 06:58 UT. There is one arch filament. Between the footpoints of the arch filament, a bright point (B_1) is observed in Hα+0.8Å. The downflow is observed at footpoints of arch filament.

(S_2) appears to be ejecting from B_{11} in the blue wing images. Arch filament 31 is lying between N_4 and P_1.

Figure 12 shows the EFR observed at 06:11 UT. The magnetic configuration is almost the same as that in figure 11. There is strong absorption in Hα blue wing images corresponding to arch filament 38. At the outer edge of penumbrae there there many bright points shown in H$\alpha\pm$0.8Å images.

4.2 Rise Velocity Evolution of Arch Filaments

4.2.1 Evolution of Two Dimensional Doppler Velocity Map

Applying Beckers' cloud model (Beckers 1964) to observed data, we obtain the Doppler velocity map of the EFR. The result maps are shown in figure 13. Comparing with Hα images, we can see that the blueshift is observed at the apex of the arch filaments and the red shift at the footpoints (e.g. 8, 9 and 10 in figure 13f). The Doppler velocity varies from -5 km s$^{-1}\sim -20$ km s^{-1} at the apex to $+20$ km s^{-1} at the footpoints.

On Day 0 (figure 13a), there are many patches of upward/downward motion, which correspond to the dark mottles in figure 3. The velocity range at the dark mottles is -20 km s$^{-1}\sim +20$ km s^{-1}.

In Day 1 images (figure 13b-e), there are two redshifted regions at the middle of images, which are corresponding to the footpoints of the EFR. At the apex of the arch
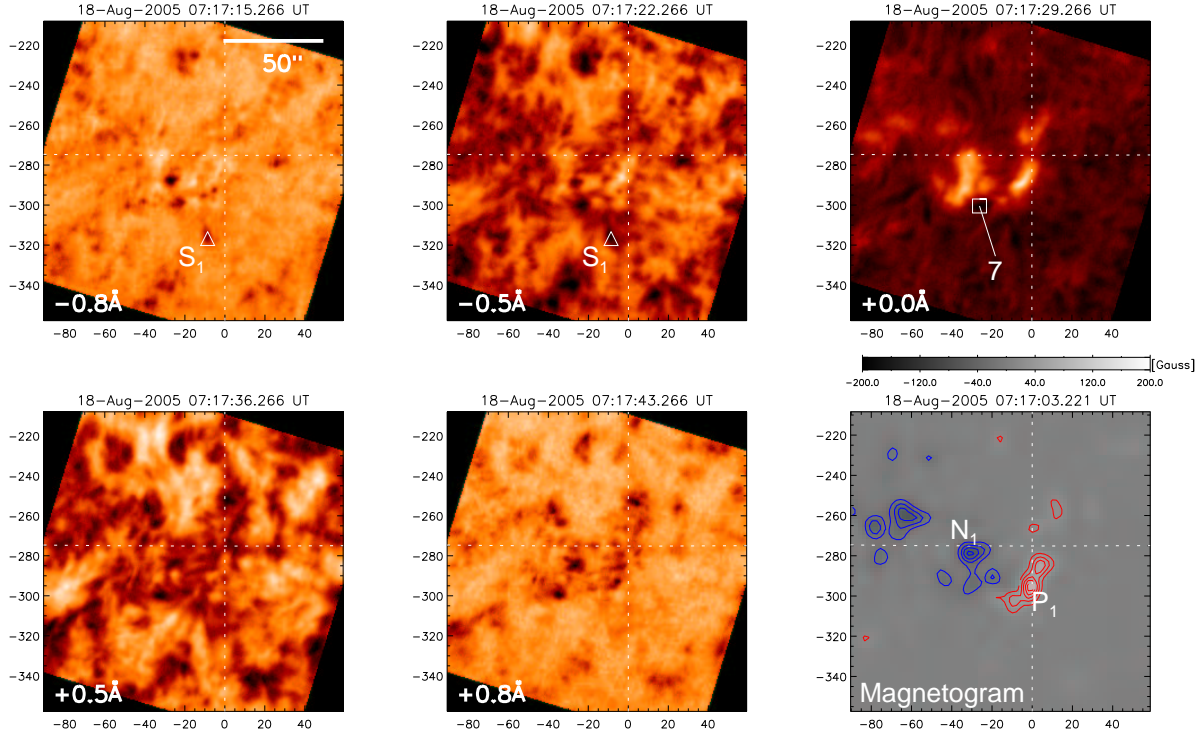
Figure 5c: The EFR observed at 07:17 UT. New arch filament 7 is emerging in Hα line center image. In the blue wing images a surge is observed (represented by S_1)

filament 1-7, the Doppler velocity is -5 km s$^{-1}\sim 15$ km s^{-1}. The downflow at the footpoints shows about $+15$ km s^{-1} redshift. In figure 13e, the surge S_1 shows blue shift of -22 km s^{-1}. There are some blueshifted area in the redshifted regions at the footpoints, where fitting to the cloud model failed because of the plages.

On Day 2, the arch filaments rise with the speed of about -3 km s$^{-1}\sim -20$ km s^{-1}. Especially, arch filament 9 and 18 show blueshift of -18 km s^{-1}. At the region between the two main spots, arch filaments rise at the speed of -3 km s$^{-1}\sim -8$ km s^{-1}. The blueshift at the plage regions is the error resulting from the fitting failure.

On Day 3 the arch filaments in figure 13j show upward motion with -15 km s$^{-1}\sim -20$ km s^{-1}. The surge S_2 in figure 13k ejects with the speed of -16 km s^{-1}. Arch filament 34 and 38 lie on the outer edge of the EFR, and present about -24 km s^{-1}. The other arch filaments in figure 13k and l show the rise velocity of -12 km s$^{-1}\sim -18$ km s^{-1}.

4.2.2   Timeplots of Contrast

To study the evolution of individual arch filaments, we plotted the time variation of contrasts for each wavelength at the apex of arch filaments (figure 14-1 and 14-2).

Among 38 arch filaments shown in figure 3-12, 12 arch filaments are chosen to plot the contrasts. There are some observational blanks in the plottings due to interruptions of the observation by cloud.

From the observed contrast we can estimate the lifetime of the arch filaments. For
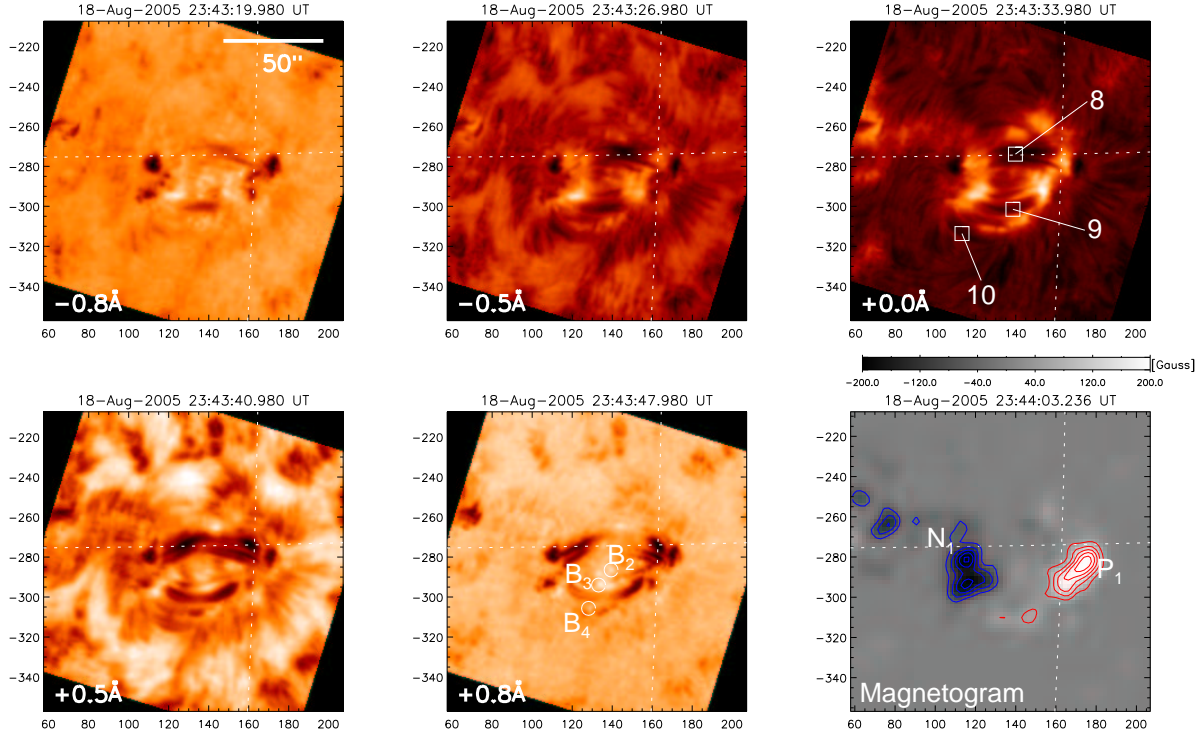
18

Figure 6: Developed EFR on Day 2. The observation time is 23:43 UT. Several arch filaments and brightening are observed. The sunspots and satellite pores are seen in Hα images. The interval of contours in the magnetogram is changed to 50 G.

example in the figure 14-1b the contrast of Hα line center is negative between 06:40 UT and 07:15 UT. From this result, the lifetime of arch filament 5 is thought to be 35 minutes. In table 2 the lifetimes of the arch filaments are shown. The arch filaments excluded from table 2 always have negative contrast of Hα line center, so we abandon the estimation of lifetime.

Table 2: The lifetime of observed arch filaments

Day #	AF #	Appearing time		Disappearing time		Lifetime
Day 1	5	August 18	06:40 UT	August 18	07:15 UT	35 m
	6		06:34 UT*		06:45 UT	∼11 m
	7		06:59 UT		07:32 UT	33 m
Day 3	23	20	00:12 UT	20	00:32 UT	20 m
	37		06:30 UT		07:04 UT	34 m

* The arch filament have appeared before the observation started.

Arch filament 29 (figure 11) has been observed for over two hours and appeared in figure 12 as arch filament 35. In the timeplot of arch filament 29 (figure 14-2j), it shows strong absorption in Hα−0.5Å for the entire time range the plot.

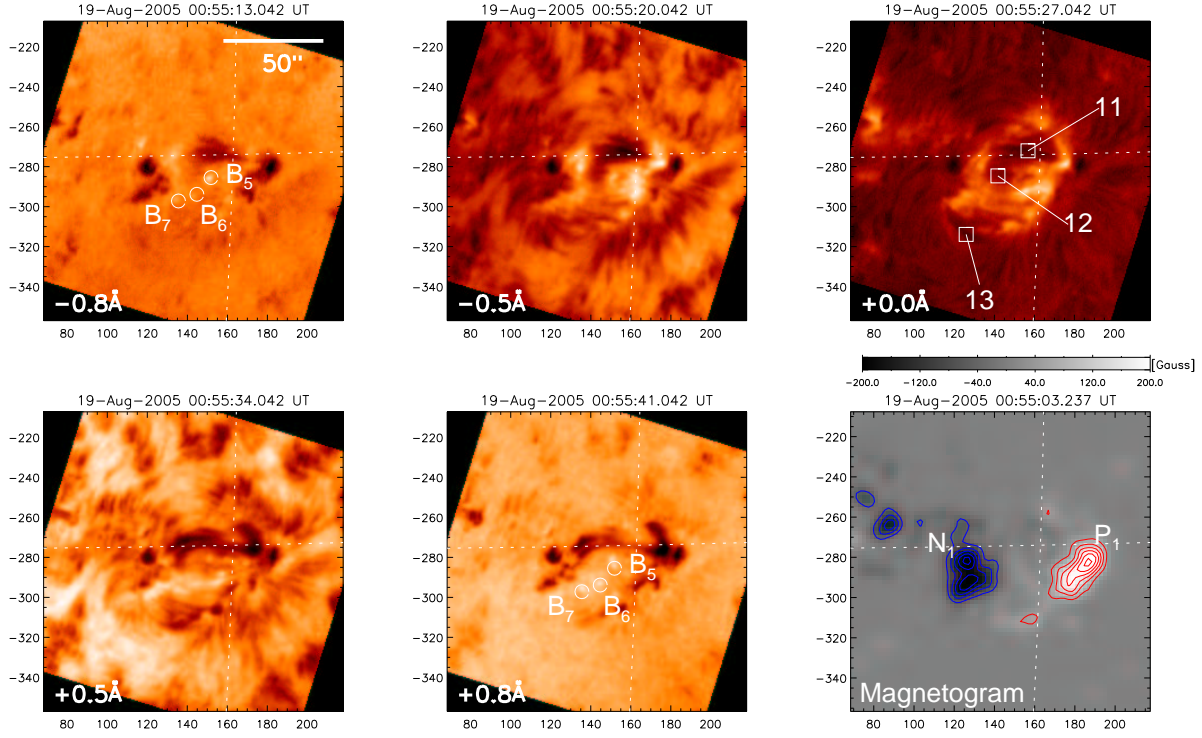In the contrast plotting of arch filament 38 shows sudden decrease of contrasts in the

19

Figure 7: The EFR observed 00:55 UT on 19 August. Three arch filaments (11, 12 and 13) are shown. The bright points locate between the footpoints.

blue wing between 06:00 UT and 06:20 UT, when the

4.2.3 Timeplot of Doppler Velocity

Applying cloud model to the plotted contrast data shown in figure 14-1 and 14-2, we derived the Doppler velocities of the arch filaments. Figure 15-1 and 15-2 shows the time variation of Doppler velocities at the apex of each arch filament.

Table 3 shows the maximum velocity of upward motion at the apex of the arch filaments.

The arch filaments on Day 1 shows the maximum rise velocity to be -1.8 km s^{-1} ~ -15.0 km s^{-1}. The velocity of arch filament 6 is fairly small, because the size of the arch filament is small and the contrast of the apex are compounded with the footpoint contrast. The upward motion lasted for about 12 minutes $\sim$ 26 minutes.

On Day 2, the maximum rise velocity varies from -5.5 km s^{-1} ~ -6.6 km s^{-1}. The positions of arch filament 11, 14 and 18 are same in the EFR.

Among the arch filaments on Day 3, filament 37 shows small value of rise velocity. On the other hand arch filament 38 has the large velocity of -20.1 km s^{-1}.

4.2.4 Magnetic Field Evolution

Figure 16 shows the evolution of the EFR observed MDI magnetogram. In figure 16a, the distance between two magnetic polarities is shown. The projection effect is removed.
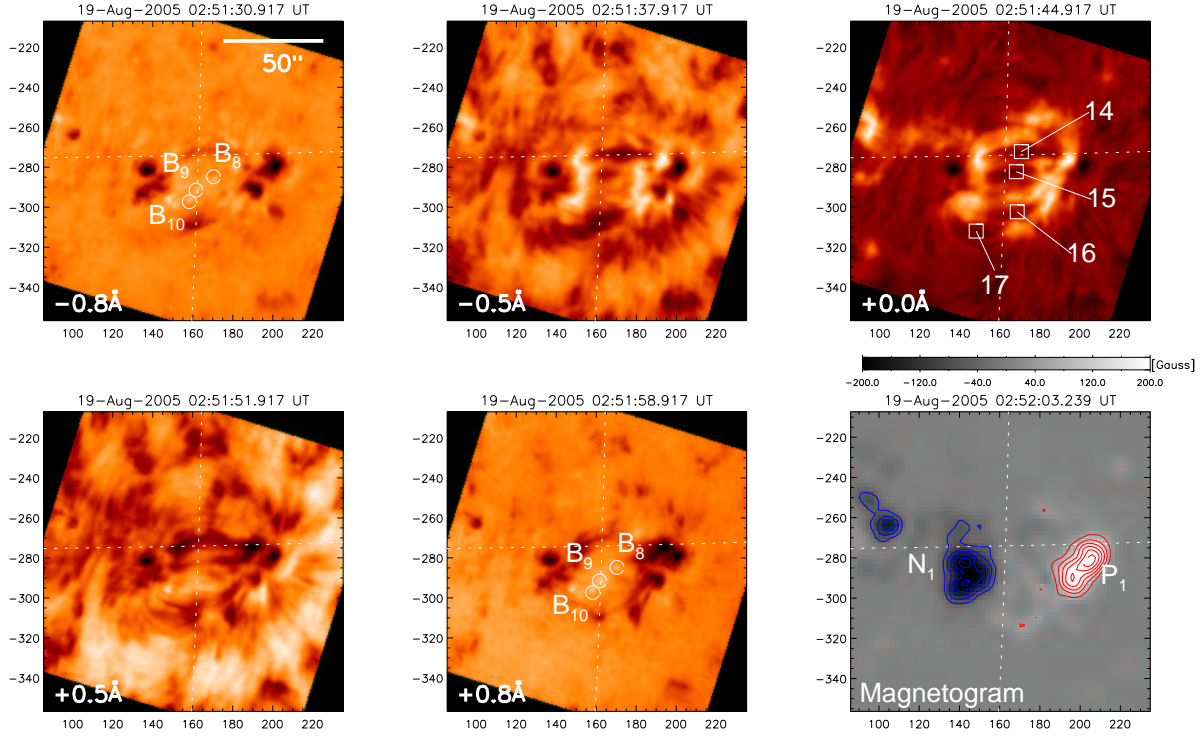
20

Figure 8: The EFR observed 02:51 UT. There are 4 arch filaments seen in Hα line center image. Some bright points exist in Hα±0.8Å images.

Table 3: The maximum rise velocity of the arch filaments

Day #	AF #	Observation time		Max velocity
Day 1	4	August 18	06:50 UT	-15.0 km s^{-1}
	5		06:47 UT	-10.7 km s^{-1}
	6		06:36 UT	-1.8 km s^{-1}
	7		07:15 UT	-5.9 km s^{-1}
Day 2	11	19	01:02 UT	-5.5 km s^{-1}
	14		03:31 UT	-8.3 km s^{-1}
	18		04:28 UT	-6.6 km s^{-1}
Day 3	23	20	00:32 UT	-11.2 km s^{-1}
	25		00:12 UT	-12.1 km s^{-1}
	29		05:18 UT	-10.0 km s^{-1}
	37		06:09 UT	-6.2 km s^{-1}
	38		06:05 UT	-20.1 km s^{-1}

From this plot, we can see the separation rate of the EFR along the flux axis. When the EFR appeared on the solar surface, the size is $20'' \approx 14$ Mm. During Day 1 the distance between the polarities increases with the speed of 0.19 km s^{-1}. On Day 2, the separation speed is accelerated to more than 0.28 km s^{-1}. Accompanied with the acceleration, the magnetic field strength at the footpoints of EFR increases in figure 16c. On Day 3 the
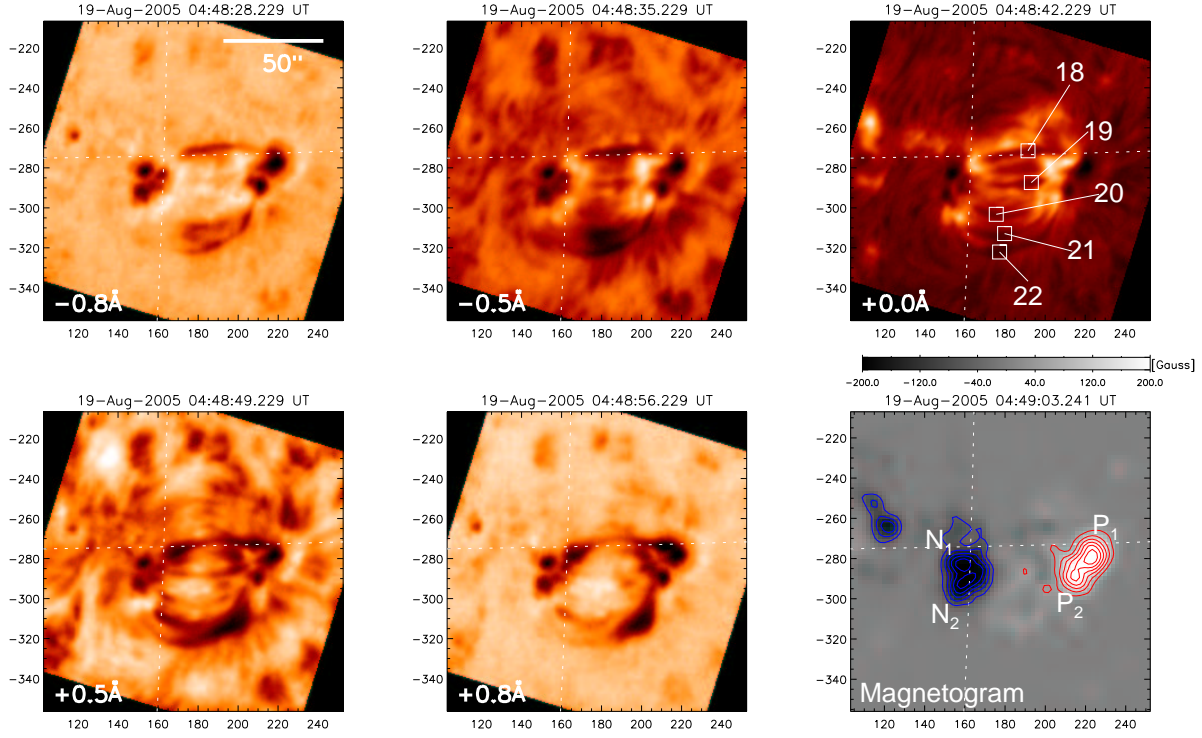
21

Figure 9: The EFR observed 04:48 UT on 19 August. New spots (N$_2$ and P$_2$) are formed south of each polarity. There are 5 arch filaments lying between the polarities. Arch filament 18, 21 and 22 are activated and visible in Hα wing images.

separation slows down to 0.03 km s^{-1}.

Figure ref1-fig16b shows the orientation angle of magnetic axis measured from the solar north toward east (counterclockwise). As we mentioned, this EFR has opposite magnetic bipole to the other ARs of the same hemisphere. The magnetic vector of the EFR pointed north-east direction when the magnetic polarities appear on the solar surface. Then the orientation angle increases and magnetic axis become parallel to the latitude lines at 19 00:00 UT (see figure 6 and 7). Finally the magnetic axis of the EFR was rotated about 60 degrees from the beginning of emergence.

In the figure 16d, the evolution of the total flux of each polarity is shown. The total flux increase gradually until 16:00 UT on August 17. Then the increasing rate of the total flux become greater than before. At the turning point of increasing rate the emergence of satellite spots began to actively occur.

5   Discussion and Summary

We observed an EFR from its appearance to the solar surface until the formation of an active region which has the sunspots with the penumbrae. The reason why the EFR didn't follow to the Hale's low is not clear. Perhaps there is relation between the EFR and preexisting AR NOAA 10978.

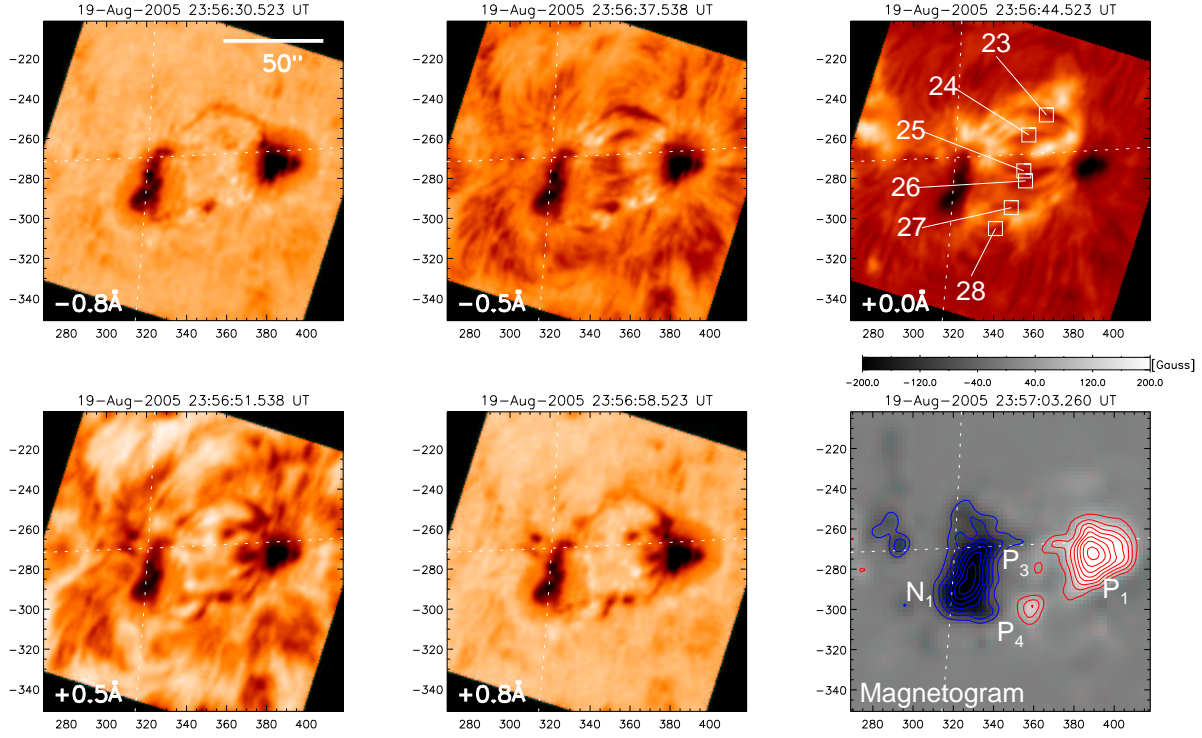The arch filaments at the initial phase of emergence show the velocity of about -15

Figure 10: The ERF observed on Day 3. The observation time is 23:56 UT on August 19. The main sunspots developed and have penumbrae.

km s^{-1}, which is near the upper limits of the range (-5 kms ~ -20 kms) obtained by the previous works (Bruzek 1969; Roberts 1970; Zwaan 1985; Chou and Zirin 1988). As the emergence advanced, the upward motion at the center of region seems to be suppressed. Instead, the emergence of arch filaments toward the outer edge of EFR appears to be activated. The arch filaments located at the outer edge shows large velocity of rising. The explanation for this velocity variation is that the magnetic pressure of pre-emerged arch filaments suppresses the rise motion of following arch filaments. Then the suppressed arch filaments are pushed laterally toward the outer edge of the EFR, where the magnetic pressure weakens and the arch filaments come to be able to rise vertically.

There are many bright points between the main polarities. Some of them are observed in Hα wing images but invisible in Hα line center images. These bright points are thought to be Ellerman bombs.

The lifetime of the arch filaments is obtained to be 11-35 minutes. On the other hand there are arch filaments observed for hours. There is an explanation that the flux tubes below the photosphere emerge one after another at the same place of the solar surface.

The summary of this study is shown below.

1. Applying Beckers' cloud model to the EFR observed by SMART, the rise velocity of arch filaments in the EFR ware obtained. The range of rise velocity is -1.8 km s^{-1} ~ -20.1 km s^{-1}. At the center of the EFR, the rise velocity of arch filaments decrease as the emergence advances. In the latter phase of the emergence, fast rising motions are observed in the arch filaments at the outer edge of the EFR.
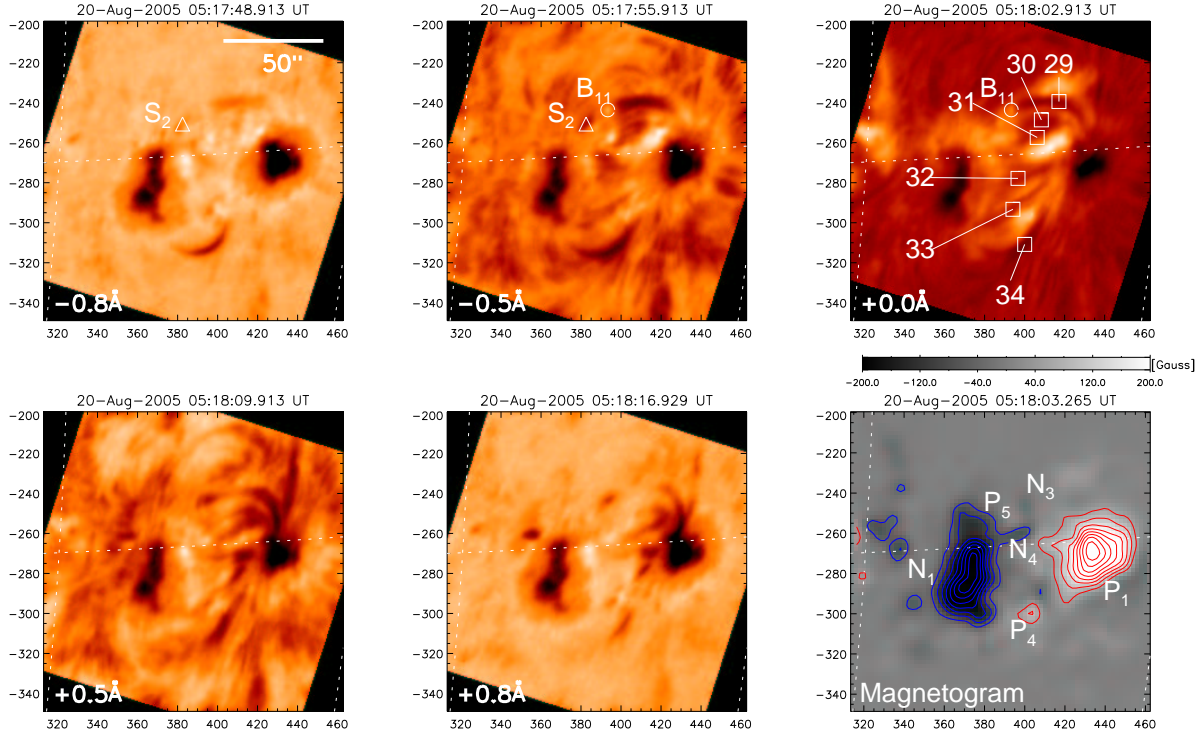
23

Figure 11: The observation time is 05:18 UT on August 20. A bright B_{11} point exists the magnetic neutral line between N_3 and P_5, from where a surge (S_2) is ejecting.

2. The lifetime of arch filaments is 11-35 minutes. There are some arch filaments seems appear to have long lifetime.

3. From MDI magnetogram data, the evolution of the distance between two polarities are obtained. The orientation angle of bipole axis shows the 60 degrees rotation during the emergence. The magnetic field strength and total flux at the footpoint of the EFR are plotted.

Appendix 1   Beckers' Cloud Model

Beckers' cloud model (Beckers 1964) considers a feature which we are looking at as a "cloud" overlying an uniform background (figure A1). The cloud is fully apart from the underlying chromosphere so that we can separate the observed intensity into the contribution from the background and the cloud.

In this model, the source function S is regarded as constant along the line-of-sight. So the radiative transfer equation inside the cloud is described as

$$I(\Delta\lambda) = S\left\{1 - \exp[-\tau(\Delta\lambda)]\right\} + I_0(\Delta\lambda)\exp\left[-\tau(\Delta\lambda)\right], \tag{A1}$$
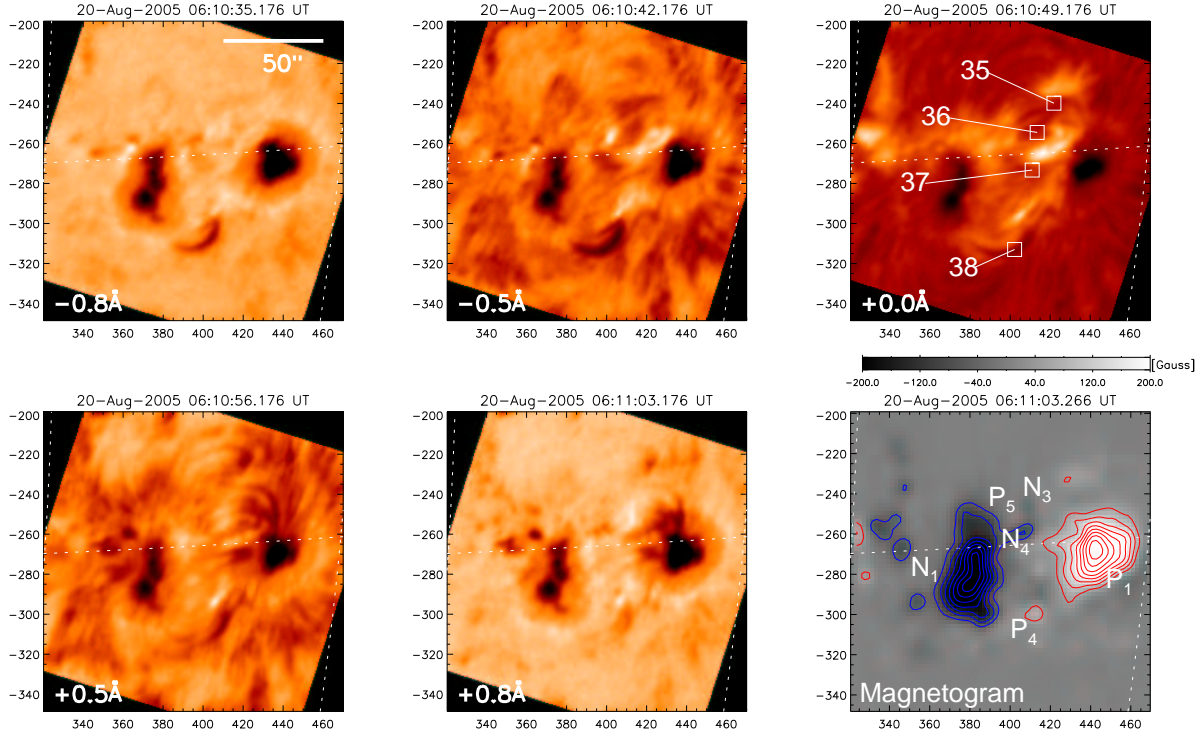
24

Figure 12: The observation time is 06:11 UT on August 20. There are 4 arch filaments. Arch filament 38 shows large upward motion in the blue wing images. The other arch filaments are fairly quiet.

where $\tau(\Delta\lambda)$ is the optical depth and written as

$$\tau(\Delta\lambda) = \tau_0 \exp\left[-\left(\frac{\Delta\lambda - \Delta\lambda_{\mathrm{I}}}{\Delta\lambda_{\mathrm{D}}}\right)^2\right]. \tag{A2}$$

In equation (A2) τ_0 is the optical depth at Hα line center, $\Delta\lambda_{\mathrm{I}}$ and $\Delta\lambda_{\mathrm{D}}$ are Doppler width and Doppler shift of Hα line, respectively. From (A1) we defined contrast $C(\Delta\lambda)$ as follows;

$$
\begin{aligned}
C(\Delta\lambda) &\equiv \frac{I(\Delta\lambda) - I_0(\Delta\lambda)}{I_0(\Delta\lambda)} \\
&= \left[\frac{S}{I_0(\Delta\lambda)} - 1\right]\left\{1 - \exp\left[-\tau(\Delta\lambda)\right]\right\}.
\end{aligned}
\tag{A3}
$$

Equation (A2) and (A3) show that the radiation from the cloud can be described by 4 parameters; S, τ_0, $\Delta\lambda_{\mathrm{D}}$ and $\Delta\lambda_{\mathrm{I}}$.

References

Banos, G. J., & Macris, C. J. 1970, Sol. Phys., 12, 106

Beckers, J. M. 1964, Ph. D. Thesis, Utrecht

Brants, J. J., & Steenbeek, J. C. M. 1085, Sol. Phys., 96, 229

Bruzek, A. 1967, Sol. Phys., 2, 451

Bruzek, A. 1969, Sol. Phys., 8, 29

Chou, D., & Zirin, H. 1988, ApJ, 333, 420

Frazier, E. N. 1972, Sol. Phys., 26, 130

Hale, G. E., Ellerman, F., Nicholson, S. B., Joy, A. H. 1919, ApJ, 49, 153

Hagenaar, H. J. 2001, ApJ, 555, 448

Harvey, K. L., & Martin, S. F. 1973, Sol. Phys., 32, 389

Heyvaerts, J., Priest, E. R., & Rust, D. M. 1977, ApJ, 21, 123

Ishii, T. T., Nagata, S., UeNo, S., Kitai, R., & Kurokawa, H., with SMART-Team 2004, ASP
    Conference Series, 325, 331l

Kurucz, R. L. 2005, Mem. S.A.It. Suppl., 8, 189

Loughhead, R. E., & Bray, R. J. 1961, Australian J. Phys., 14, 347

Lyot, B. 1944, Ann, d'Astrophys. 7, 21

Macris, C. J. 1957, Ann Astrophys., 49, 73

Matsumoto, R., & Shibata, K. 1992, PASJ, 44, 167

Miller, R. A. 1960, J. Brit. Astron. Assoc., 70, 100

Murry, N. 1992, ApJ, 401, 386

Otsuji, K., et al. 2007, PASJ, 59, 649

Perker, E. N. 1966, ApJ, 145, 491

Perker, E. N. 1969, Space Sci. Rev., 9, 651

Perker, E. N. 1978, ApJ, 221, 368

Powell, M. J. D. 1970, Gordon and Breach, 115

Roberts, P. H. 1970, Ph. D. Thesis, Calif. Inst. Of Technology

Shibata, K., Tajima, T., Matsumoto, R., Horiuchi, T., Hanawa, T., Rosner, R., & Uchida, Y.
    1989, ApJ, 338, 471

Shibata, K., Tajima, T., Steinolfson, R.S., & Matsumoto, R. 1989, ApJ, 345, 584

Shibata, K., et al. 1992a, PASJ, 44, L173

Shibata, K., Nozawa, S., & Matsumoto, R. 1992b, PASJ, 44, 265

Shibata, K. 1998, Ap&SS, 264, 129

Shimizu, T., shine, R. A., Title, A. M., Tarbell, T. D., & Frank, Z. 2002, ApJ, 574, 1074

Spruit, H. C., 1979, Sol. Phys., 61,363

Strous, L.H., Scharmer, G., Tarbell, T.D., Title, A., M., & Zwaan, C. 1996, A&A, 306, 947

Tsiropoula, G., Georgakiilas, A. A., Alissandrakis, C. E., & Mein, P. 1992, A&A, 22, 587

Zirin, H. 1972, Sol. Phys., 22, 34

Zwaan, C. 1978, Sol. Phys., 60, 213
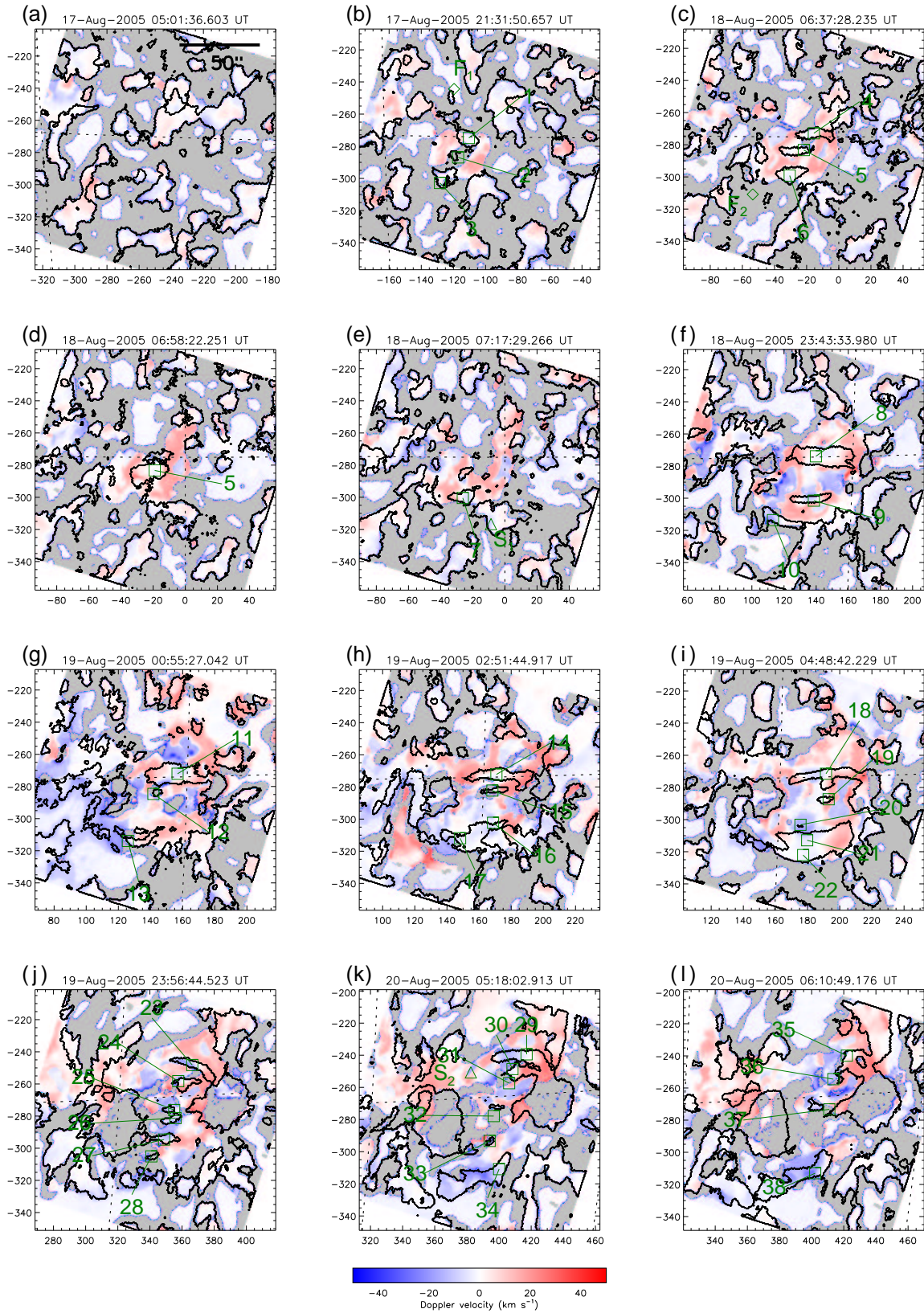
Zwaan, C. 1985, Sol. Phys., 100, 397

Figure 13: The Doppler velocity maps obtained from the observed data shown in figure 3-12. The blue area shows the upward (approaching) motion and red area shows the downward motion. The gray area represent the region where the fitting to the cloud model is not carried out. The black line shows the contour map of the contrast averaged through the wavelengths. The arch filaments, filaments and surges are presented by green labels.
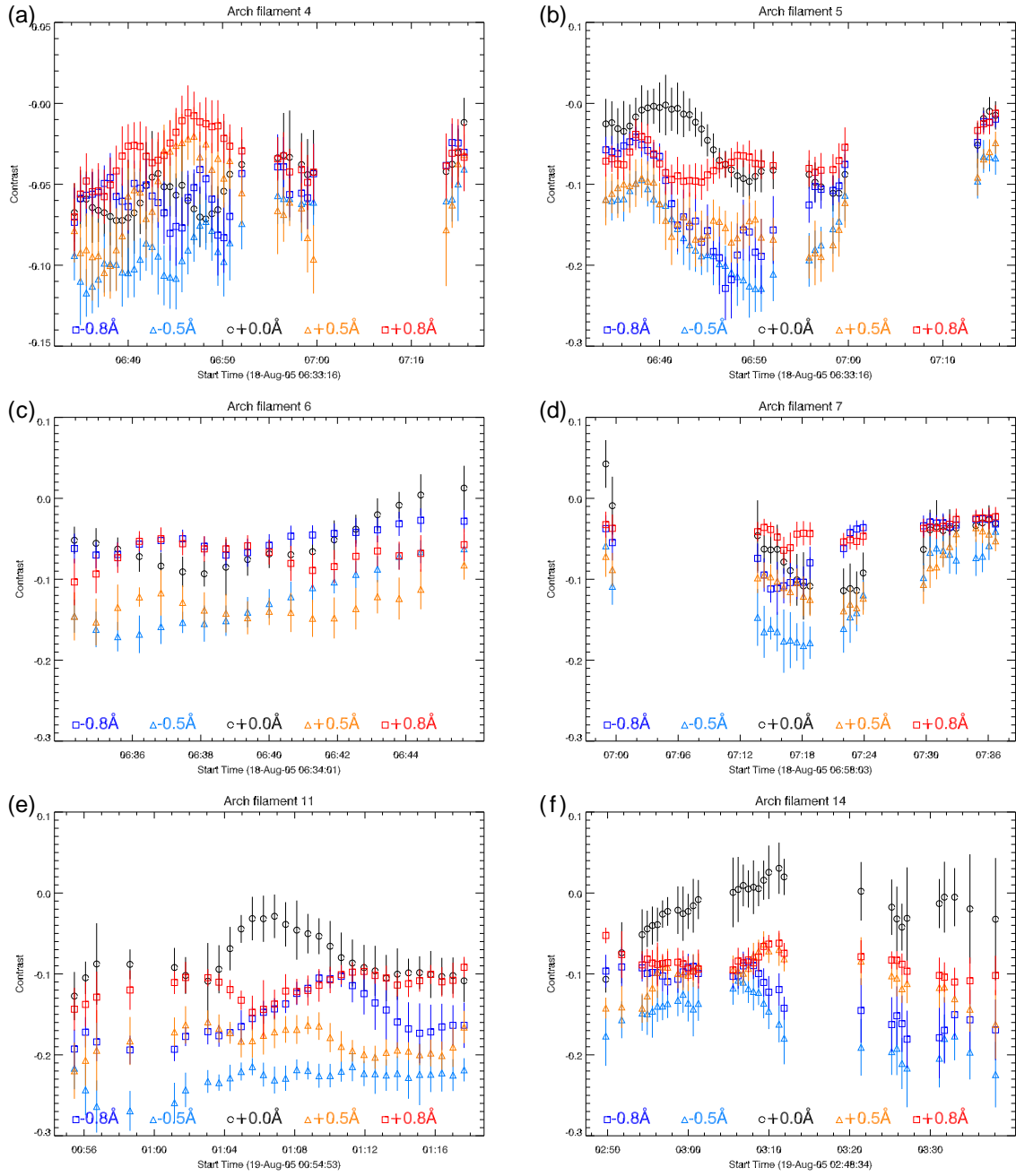
28

Figure 14-1: The timeplots of contrasts for each wavelength on the arch filaments. 12 arch filaments are selected to plot the contrasts. The filament number is shown above each panel.
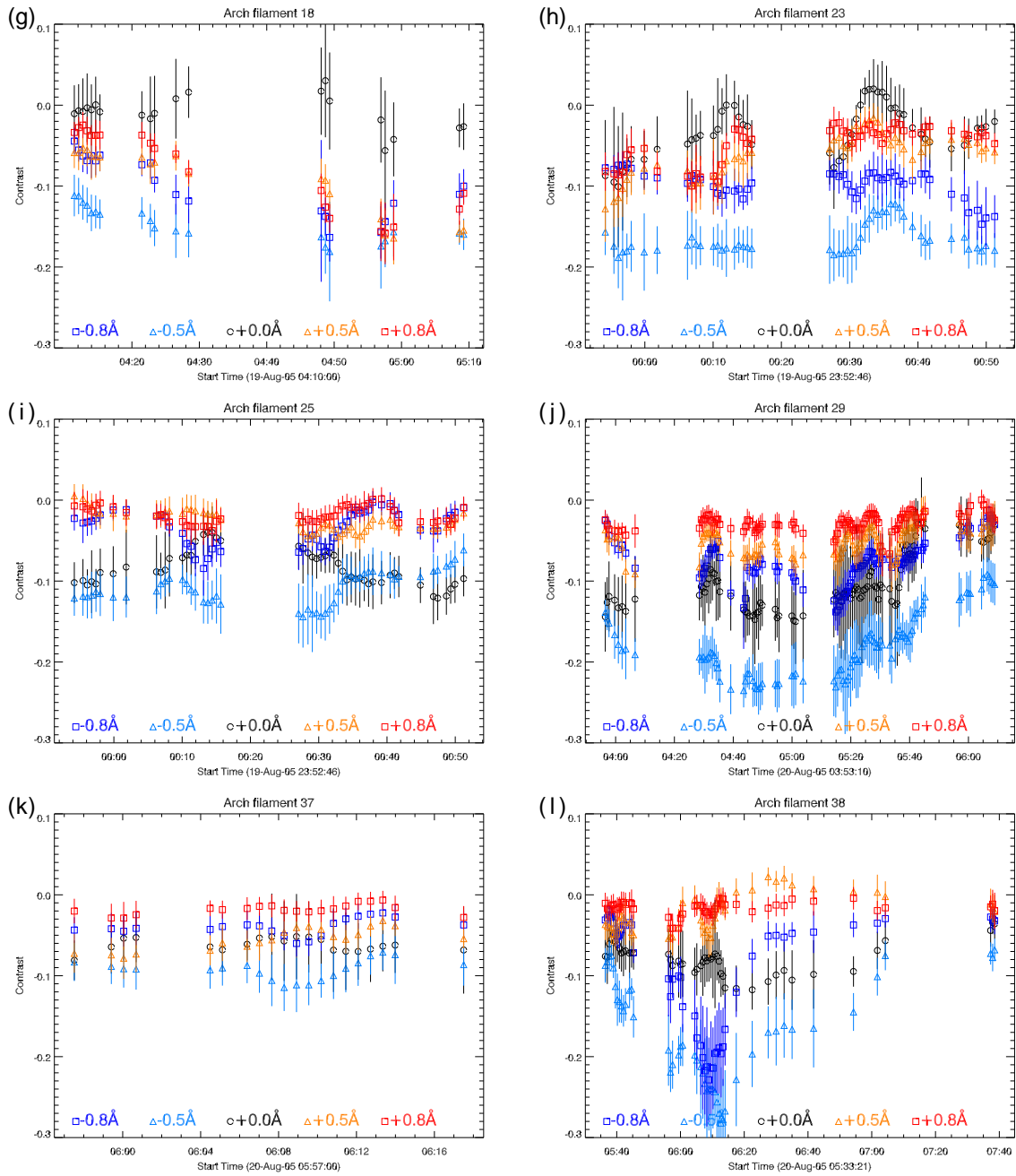
29

Figure 14-2: The continuation of figure 14-1. Note that the scale of vertical and abscissa axis differs among each panel. The correspondence between plotting color and wavelength is shown bottom in each timeplot.
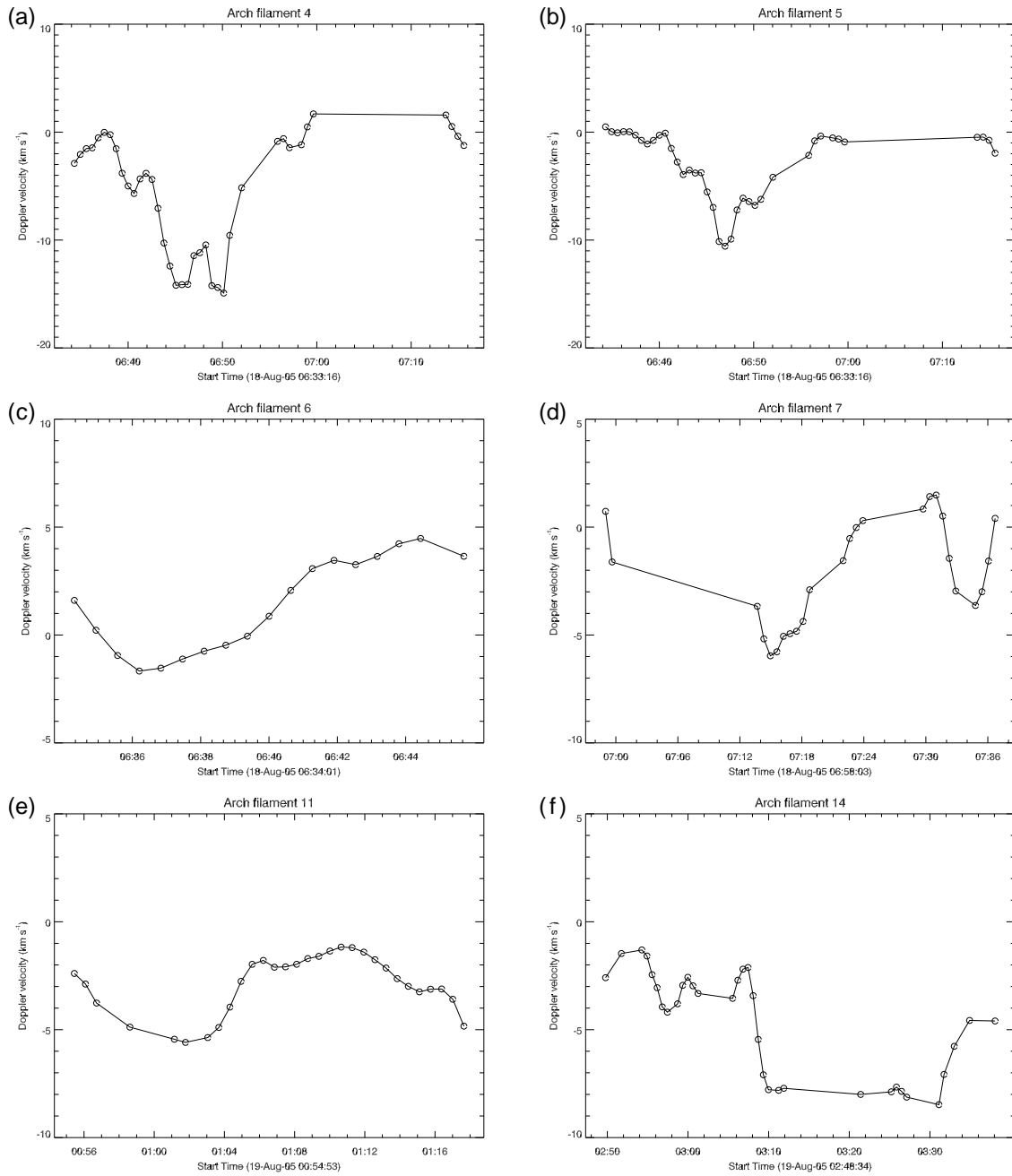
30

Figure 15-1: The timeplots of Doppler velocities the arch filaments. Positive value represents redshift, negative value corresponds to blueshift.
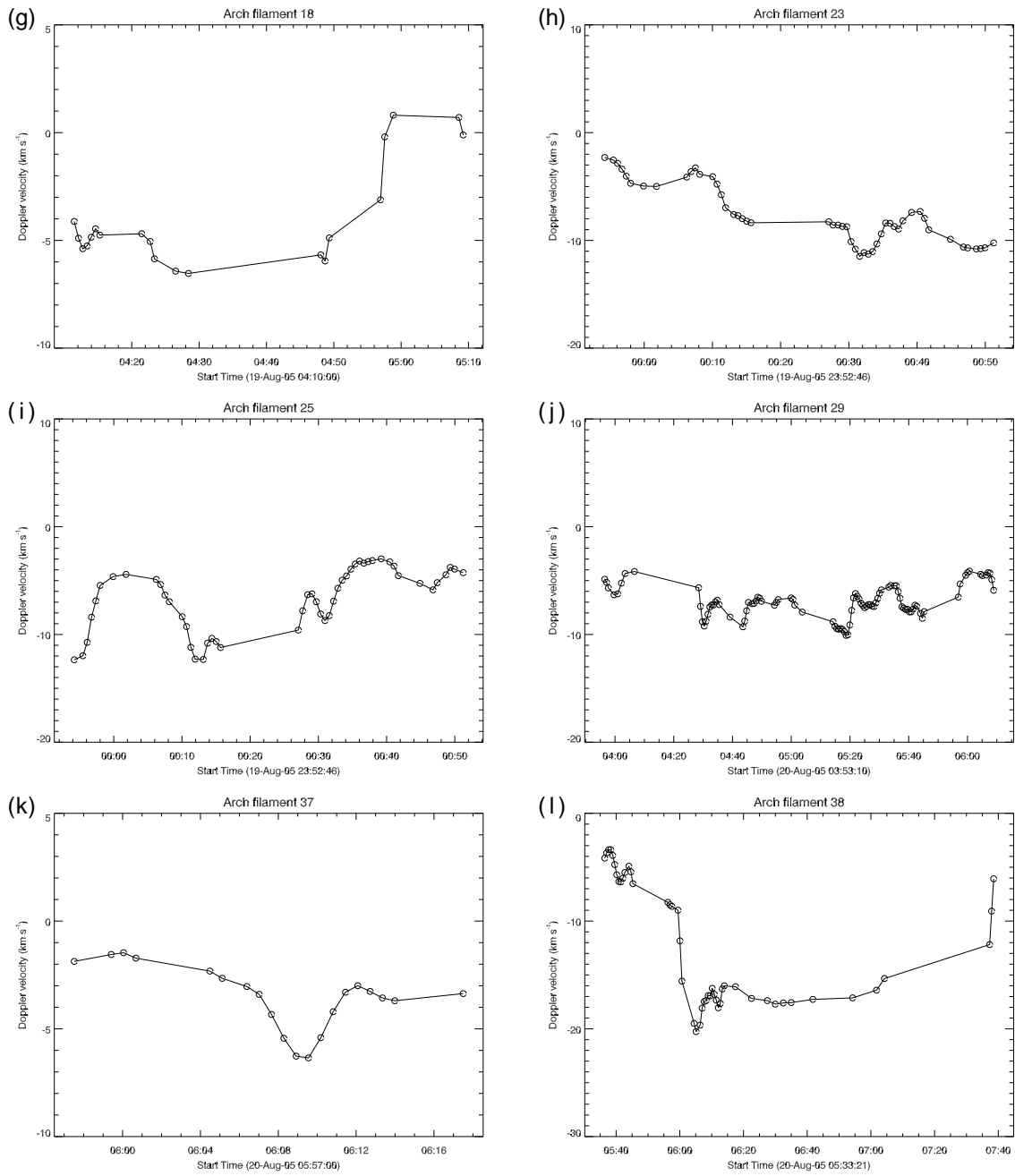
31

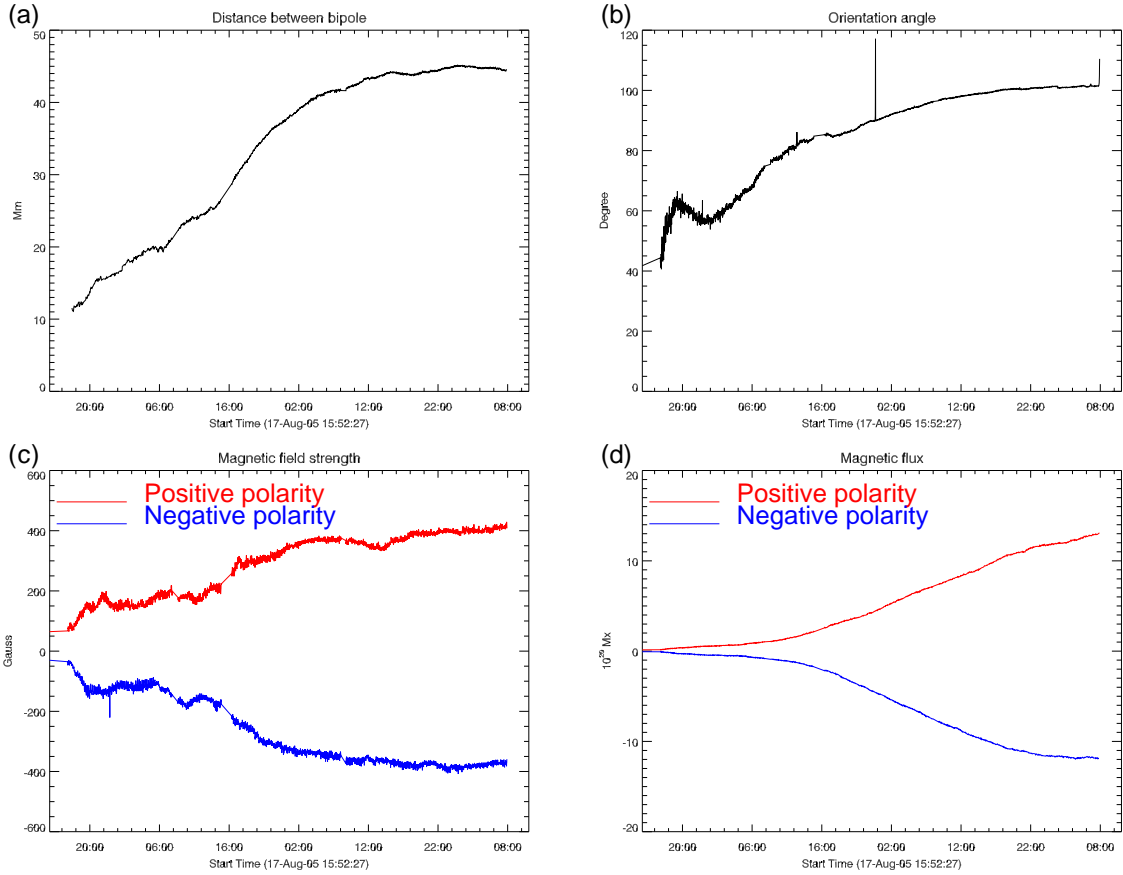Figure 15-2: The continuation of figure 15-1.

Figure 16: The evolution of magnetic characteristics. Upper left panel: the distance between the opposite polarities. Upper right panel: the orientation angle of the magnetic bipole against the solar north (counter-clockwise: +). Lower left panel: the magnetic field strength at the centroids of the main polarities. Lower right panel: the total flux of each polarity.
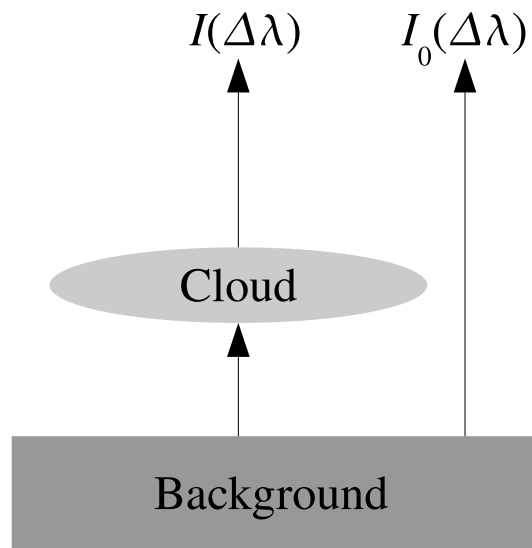
33

Figure A1: Picture of Beckers' cloud model. The "cloud-like" feature is above the uniform background chromosphere. $I(\Delta\lambda)$ and $I_0(\Delta\lambda)$ are intensity from the cloud and background, respectively. $\Delta\lambda$ is the difference between the observational wavelength and Hα line center.

Part II
Small Scale Magnetic Flux Emergence Observed with Hinode / Solar Optical Telescope

Abstract

We observed small scale magnetic flux emergence in a sunspot moat region by the Solar Optical Telescope (SOT) aboard the Hinode satellite. We analyzed filtergram images observed in the wavelengths of Fe 6302 Å, G-band and Ca II H. In Stokes I images of Fe 6302 Å, emerging magnetic flux were recognized as dark lanes. In G-band, they showed their shapes almost the same as in Stokes I images. These magnetic flux appeared as dark filaments in Ca II H images. Stokes V images of Fe 6302 Å showed pairs of opposite polarities at footpoints of each filament. These magnetic concentrations are identified to correspond to bright points in G-band/Ca II H images. From the analysis of time-sliced diagrams, we derived following properties of emerging flux, which are consistent with the previous works. (1) Two footpoints separate each other at a speed of 4.2 km s^{-1}during the initial phase of evolution and decreases to about 1 km s^{-1}in 10 minutes later. (2) Ca II H filaments appear almost simultaneously with the formation of dark lanes in Stokes I in the observational cadence of 2 minutes. (3) The lifetime of the dark lanes in Stokes I and G-band is 8 minutes, while that of Ca filament is 12 minutes.

An interesting phenomena was observed that an emerging flux tube expands laterally in the photosphere with a speed of $3.8\,\mathrm{km\,s^{-1}}$. Discussion on the horizontal expansion of flux tube will be given with reference to previous simulation studies.

1   Introduction

Emerging flux region (EFR) is a young active region (AR) where magnetic flux loops emerge from underneath photosphere (Bruzek 1969; Zirin 1972). Emerging flux often causes reconnection with preexisting coronal magnetic field and are responsible to flares (Heyvaerts et al. 1977; Shibata et al. 1992a; Shibata et al. 1992b; Shibata 1999; Shimizu et al. 2002). The morphological features of emerging flux observed in Hα are dark loops and bright points near their footpoints. A cluster of dark loops is named as an "arch filament system" (AFS) by Bruzek (1967). A single arch filament is thought to be a trace of a magnetic flux tube. The lifetime of an arch filament is 10-30 minutes and the rise velocity is 10-15 km s^{-1}(Chou and Zirin 1988). Evolutions of emerging flux from the chromosphere to the corona were investigated by Yoshimura and Kurokawa (1999) and Shimizu et al. (2002). They observed that emerging flux appeared in soft X-ray images about several minutes after the appearance of new arch filament in Hα images.

Shibata et al. (1989) performed two dimensional magneto-hydrodynamic (MHD) simulations of emerging flux for the first time, which reproduced well various dynamical features of emerging flux, such as the rise motion of an arch filament and donwflow along

it. Subsequently, three dimensional simulations of emerging flux have been carried by Matsumoto and Shibata (1992) and others (Matsumoto et al. 1993; Fan 2001; Magara and Longcope 2001; Nozawa 2005). These three-dimentional simulations showed that when there is no strong magnetic twist, the emerging flux undergoes strong horizontal expansion in a direction perpendicular to emerging flux filament just after its emergence into the photosphere, which are remained to be confirmed by actual observations.

Recently Pariat et al. (2004) proposed a new way of emergence from the flare genesis experiment observation that emerging flux rises in a form of undulatory loops in the photosphere, which must be confirmed observationally by many samples of EFRs. In this paper, we report the result of our analysis of an EFR observed by the Solar Optical Telescope (SOT) on board Hinode. Thanks to multi-wavelength observation from space (Kosugi et al. 2007; Tsuneta et al. 2007; Suematsu et al. 2007; Ichimoto et al. 2007; Shimizu et al. 2007), we could follow the temporal evolution of emerging loops in the photosphere and the chromosphere. Our analysis is concentrated on (1) morphological evolution of an EFR in and below the chromospheric layers and (2) basic morphological characters of individual emerging loops.

2   Observation and data reduction

2.1   Observation

Fig. 1 shows an EFR appeared in the moat region of NOAA 10930 near the disk center (E08°S05°) on December 19, 2006 with Hinode/SOT. The observation was done from 17:00 to 19:00 UT. In this period, many small scale EFRs were observed at the southwest part of the region.

Multi-wavelength imaging observation was done in three wavelengths, i.e., (1) Fe 6302 Å Stokes I and V, (2) G-band 4305 Å, and (3) Ca II H 3968.5 Å. The observational cadence was 2 minutes. The images in (1) were taken through the narrow-band filter imager (NFI) with the pass-band of 90mÅ, while the images in (2) and (3) through the broad-band filter imager (BFI) with the pass-band of 0.8Å and 0.3Å, respectively. In our observation, spatial resolutions are $0''.16$/pixel (NFI) and $0''.10$/pixel (BFI).

2.2   Data reduction

Co-alignment between NFI and BFI images were done with reference to common granulation patterns. To derive basic morphological properties of emerging loops, we made two kind of time-sliced diagrams similar to Shimizu et al. (2002). One is "along-filament" and the other is "trans-filament" time-sliced diagram, as is described in Fig. 2.

Fig. 3 and 4 shows the ways how to measure the various size of an emerging loop. In this study, we analyzed the evolutions of (1) the linear size of the footpoints of emerging loop, (2) the distance between the footpoints, and (3) the length and width of dark lane or filament.
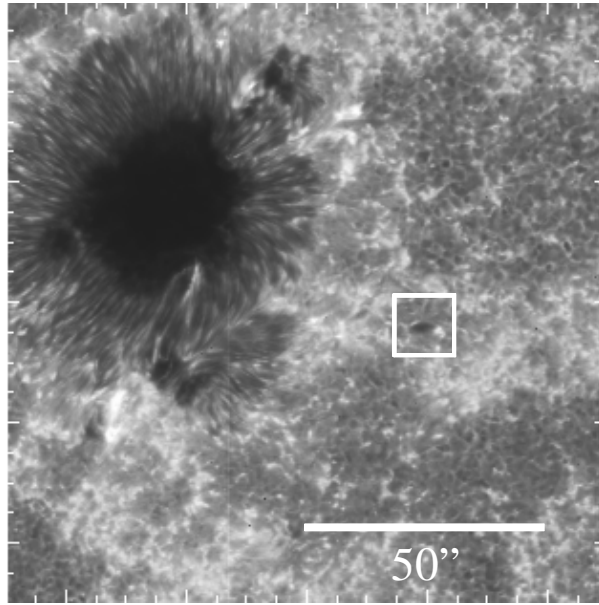
Figure 1: Ca II H line image of NOAA 10930 obtained by Hinode/SOT at 18:01:52 UT on December 19, 2006. An EFR indicated by a white square was studied.
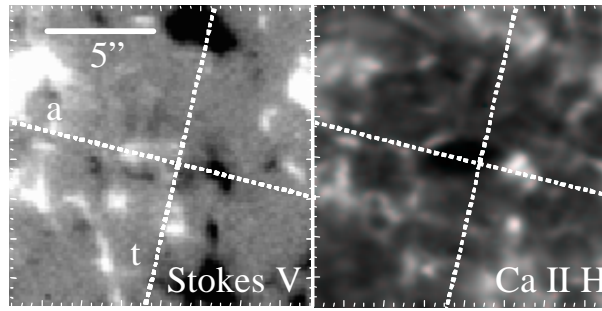

Figure 2: The emerging flux observed i./part2/n Fe 6302 Å Stokes V (left panel) and Ca II H (right panel). Two dashed lines are drawn to represent the position of two slits for time-sliced diagrams. Slit a is drawn on the two footpoints of the emerging flux (along-filament). Slit t is perpendicular to the slit a and put on the midpoint of the two footpoints (trans-filament).

3 Morphological characteristics of the EFR

3.1 Before the emergence of the flux tube

Fig. 5 shows images of the flux tube at three stages of its emergence. The upper 4 images are taken at 17:25:51 UT, when the flux emergence had not occurred yet. Before the emerging flux's appearance, there was no particular feature in each 4 images.

3.2 The initial stage of the emergence of the flux tube

The middle 4 images of Fig. 5 are taken at 18:01:52 UT, when about 8 minutes passed from the beginning of the flux emergence. In the image of Stokes I, there seems to be two dark lanes (1 and 2). The widths of the dark lanes are about $1''.5$ and lengths of them are $4''$. There is no prominent brightening at the footpoints of the emerging flux. In the image of Stokes V, we can see a pair of opposite polarities (P_1 and N_1) at the middle

Ca II H along-filament
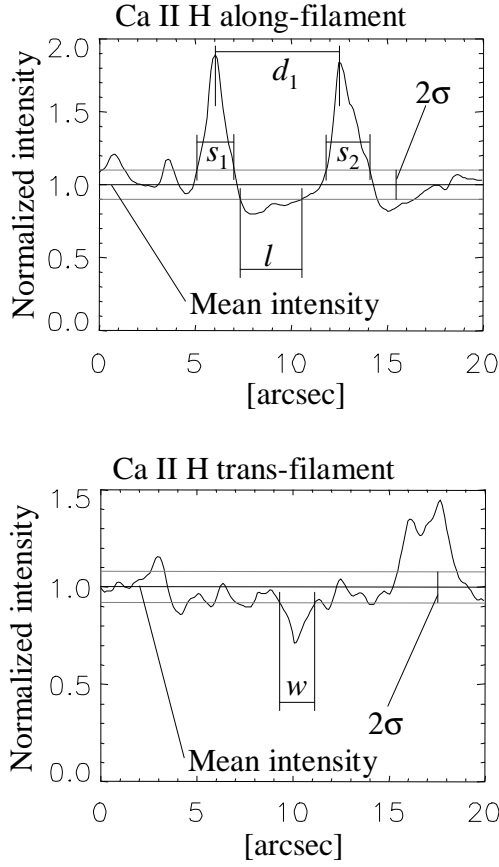

Ca II H trans-filament

Figure 3: Definition of linear size of Ca II features. The intensity distribution is normalized by the mean intensity of the neighboring quiet region. σ is the standard deviation of intensity fluctuation in the neighboring quiet region. d_1: the distance between the two intensity peaks; s_1 and s_2: the linear size of two bright points; l: the length of the filament; and w: the width of dark lane/filament. The same definition is applied to Stokes I and G-band images.
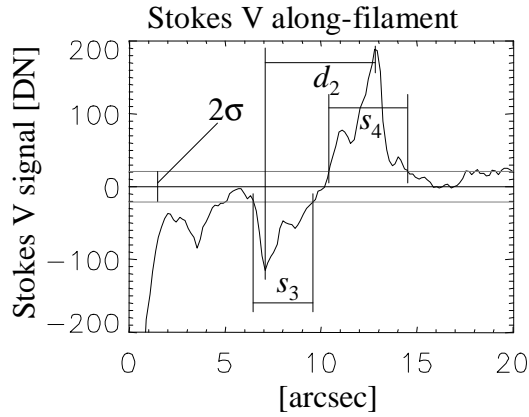
Stokes V along-filament

Figure 4: Stokes V distribution on the along-filament slit. The fluctuation of Stokes V signal on the neighborhood quiet region are expressed by σ. In the panel, d_2: the distance between two opposite polarities of magnetic flux; and s_3 and s_4: the linear size of footpoints of emerging flux.

of the image. They are the footpoints of the emerging flux. The distance between two footpoints is about $5''$. In G-band, we can identify two loops or filaments more clearly

than in Stokes I. The widths and the lengths of the arch filaments observed in G-band are almost the same as those in Stokes I. At the both ends of arch filaments, there are tiny bright points in G-band. The size of the bright points is about $0''.5 \times 0''.5$. In the image of Ca II H, the arch filaments appear darker and wider. Arch filament 1 and 2 almost merge to each other. The width of individual arch filament is about $1''$ and the whole width of arch filaments is about $2''$. The lengths of the arch filaments are about $4''$ and the same as in the other images.

3.3   The later stage of the emergence of the flux tube

The bottom 4 images in Fig. 5 show the morphology of flux tube at its later phase of emergence. The observation time is 18:11:53 UT, so 18 minutes after the emergence. In the image of Stokes I we can see four dark lanes (3, 4, 5 and 6), while there are no longer any dark lanes which connect directly between the original footpoints. The widths of these dark lanes are about $0''.7$ and the length of each dark lane is about $2''$-$3''$. In the image of Stokes V, the distance between two opposite polarities is $7''$ and larger than 10 minutes ago. Note that in the middle region between the originally emerged footpoints there are several small magnetic concentrations (p_1, n_1, p_2 and n_2). Same as in Stokes I image, there are four arch filaments in G-band image. The values of the width and length of arch filaments are also same as those of Stokes I. The size of the bright points at the footpoints is about $1'' \times 1''$. In Ca II H image we can see four arch filaments, same as the other images. The width of each arch filament is about $0''.5$, and the length of them is $2''$-$3''$. At the middle of two main footpoints it forms new footpoints of the arch filaments. While the size of the bright points at the main footpoints is $1''.5 \times 1''.5$, those of the newly formed footpoints at the middle of the EFR is $0.''5 \times 0''.5$.

4   Temporal evolution of an emerging flux loop

In this section, we study more quantitatively the temporal evolution of individual emerging loops.

4.1   Evolution of the footpoints

Fig. 6 is the "along-filament" time-sliced diagram of an emerging loop. Temporal variation of linear sizes and mutual separation speed of footpoints measured in Stokes I and V, G-band and Ca II H are shown in Fig. 8.

From Fig. 8a, we can say that Ca bright point is larger than that of Stokes I/V and G-band features. From Fig. 8b, the same result is obtained, except Stokes V feature. As can be seen in Stokes V map of Fig. 6, there was a pre-existing negative polarity features on the slit. So the size increment of negative polarity features after the emergence correspond to real size of the footpoint of emerged loop. If so, we may conclude that the size of the Ca feature is larger than those of the photospheric features in both polarities.

The footpoints of opposite polarity move away from each other at a speed of 4.2 km s^{-1} in the initial phase, and slow down to 0.8 km s^{-1} (Fig. 8c), which is consistent with

previous work by Harvey and Martin (1973).

4.2 Evolution of the loops

of Stokes I (Fig. 6) clearly shows the dark lane which appeared at 17:54 UT and faded out at 18:02 UT. So the lifetime is 8 minutes. G-band time-sliced diagram shows the same behavior as that of the Stokes I. The first Ca arch filament (1 in Fig. 5) appeared at 17:54 UT and lasted until 18:06 UT, when in the same place two new emergence occurred (3 and 4 in Fig. 5). So the lifetime of Ca arch filament 1 is 12 minutes. The elongation speeds of Stokes I dark lane, G-band lane and Ca arch filament are of 2.9 km s^{-1}(Fig. 8d).

From the trans-filament time-sliced diagram (Fig. 7), we can see the evolution of the flux width. The dark lanes or filaments expanded laterally with the speed of 3.8 km s^{-1}in all the wavelengths observed and reached the width of $2''.0$, although the Ca II H loop lasted longer and attained the final width of $3''.5$ (Fig. 8e).

5 Discussion and summary

5.1 Discussion

We have confirmed that the Ca bright points in the chromosphere are larger than features observed in Stokes I and G-band formed in the photosphere. This can be expected if the decreasing gas pressure with height allows for an expansion of the flux tube with height.

Fig. 9 shows the model of this EFR. Temporal evolution of the observed flux emergence will be as follows: (1) A magnetic flux tube emerges from intergranular lane (17:54 UT). (2) The flux tube splits along its axis into two parts (flux tubes 1 and 2). (3) After the emergence of flux tubes 1 and 2, newly emerged flux tubes appear (flux tubes 3-6). These undulatory emergence of flux will be the ones observed by Pariat et al. (2004) and simulated by Isobe et al. (2007).

The horizontal expansion of an emerging flux tube in the photosphere was clearly detected in this work. What is the mechanism of flux tube expansion? This may correspond to the horizontal expansion of the emerging flux in the photosphere, theoretically predicted by three dimensional simulations. Matsumoto et al. (1993) simulated the emergence of non-twisted flux tube and showed that the horizontal expansion speed of flux tube is 30 km s^{-1}in the photosphere. Fan (2001) and Magara and Longcope (2001) studied the emergence of twisted flux tubes and obtained the horizontal speeds of flux tube expansion to be 6-8 km s^{-1}. Nozawa (2005) performed a comprehensive simulation of emerging magnetic flux sheets. The horizontal expansion speed of non-sheared sheets is 20 km s^{-1}, while that of sheared sheet is $\sim$10km s^{-1}. All the results of three dimensional simulations of emerging flux tubes tell us that the horizontal expansion speed will be reduced when the tubes are twisted. As our observation showed a relatively slow speed of horizontal expansion (3.8 km s^{-1}) compared with the simulational results of non-twisted tubes expansion, the flux tube studied by us is probably a twisted one.

5.2 Summary

We observed an emerging flux which appeared near NOAA 10930 with Hinode/SOT. From this study, the following properties about EFRs were found.

1. The size of Ca bright points is larger than those of Stokes I and G-band.

2. Two footpoints separate each other at the speed of 4.2 km s^{-1}during the initial phase of evolution. In later phase, the separating rate decreases to 0.8 km s^{-1}.

3. The lifetime of the dark lanes in Stokes I and G-band is 8 minutes, while that of Ca filament is 12 minutes.

4. The Ca arch filament appears within 2 minutes after the formation of the dark lane in Stokes I image.

5. The width of the Ca arch filament is $3''.5$ at its maximum, which is wider than that of the photospheric dark lanes ($2''.0$).

6. The dark lanes or filaments expand laterally with a common speed of 3.8 km s^{-1}in the photosphere and the chromosphere. Slow lateral expansion of the flux tube suggests that the flux tube is a twisted one.

Acknowledgement

References

Bruzek, A. 1967, Sol. Phys., 2, 451

Bruzek, A. 1969, Sol. Phys., 8, 29

Chou, D., & Zirin, H. 1988, ApJ, 333, 420

Fan, Y. 2001, ApJ, 546, 509

Harvey, K. L., & Martin, S. F. 1973, Sol. Phys., 32, 389

Heyvaerts, J., Priest, E. R., & Rust, D. M. 1977, ApJ, 21, 123

Isobe, H., Tripathi, D., & Archontis, V. 2007, ApJ, 657, L53

Ichimoto, K., et al. 2007, Sol. Phys., submitted

Kosugi, T., et al. 2007, Sol. Phys., submitted

Magara, T., & Longcope, D. W. 2001, ApJ, 559, L55

Matsumoto, R., & Shibata, K. 1992, PASJ, 44, 167

Matsumoto, R., Tajima, T., Shibata, K., & Kaisig, M. 1993, ApJ, 414, 357

Nozawa, S. 2005, PASJ, 57, 995

Pariat, E., Aulanier, G., Schmieder, B., Georgoulis, M. K., Rust, D. M., & Bernasconi, P. N.
    2004, ApJ, 614, 1099

Shibata, K., Tajima, T., Steinolfson, R.S., & Matsumoto, R. 1989, ApJ, 345, 584

Shibata, K., et al. 1992a, PASJ, 44, L173

Shibata, K., Nozawa, S., & Matsumoto, R. 1992b, PASJ, 44, 265

Shibata, K. 1999, Ap&SS, 264, 129

Shimizu, T., shine, R. A., Title, A. M., Tarbell, T. D., & Frank, Z. 2002, ApJ, 574, 1074

Shimizu, T., et al. 2007, Sol. Phys., submitted

Strous, L.H., Scharmer, G., Tarbell, T.D., Title, A., M., & Zwaan, C. 1996, A&A, 306, 947

Suematsu, Y., et al. 2007, Sol. Phys., submitted

Tsuneta, S., et al. 2007, Sol. Phys., submitted

Yoshimura, K., & Kurokawa, H. 1999, ApJ, 517, 964

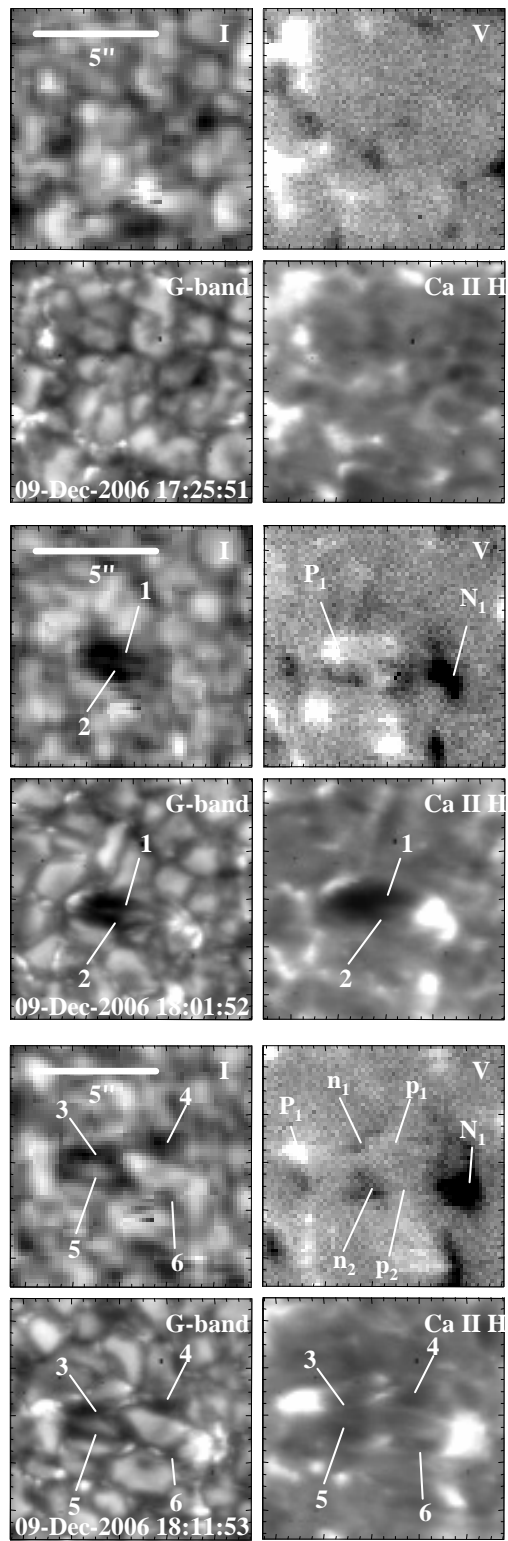Zirin, H. 1972, Sol. Phys., 22, 34

42

Figure 5: The flux tube at three stages of its emergence. (a) before the emergence. (b) the initial stage of the emergence. (c) the later stage of the emergence. In each 4 images, upper left, upper right, lower left and lower right show Fe 6302 Å Stokes I, V, G-band and Ca II images of the studied region with a common scale of magnification. In the images, the loops of the EFR and magnetic polarities at the loop's footpoints are indicated by numbers and alphabets.
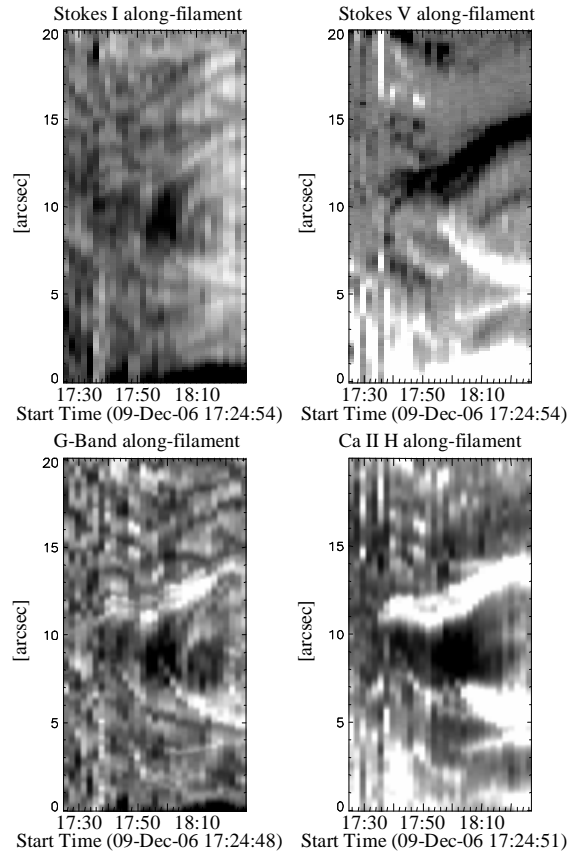
43

Figure 6: Along-filament time-sliced diagram of the emerging flux. Upper left: Stokes I, upper right: Stokes V, lower left: G-band, lower right: Ca II H.
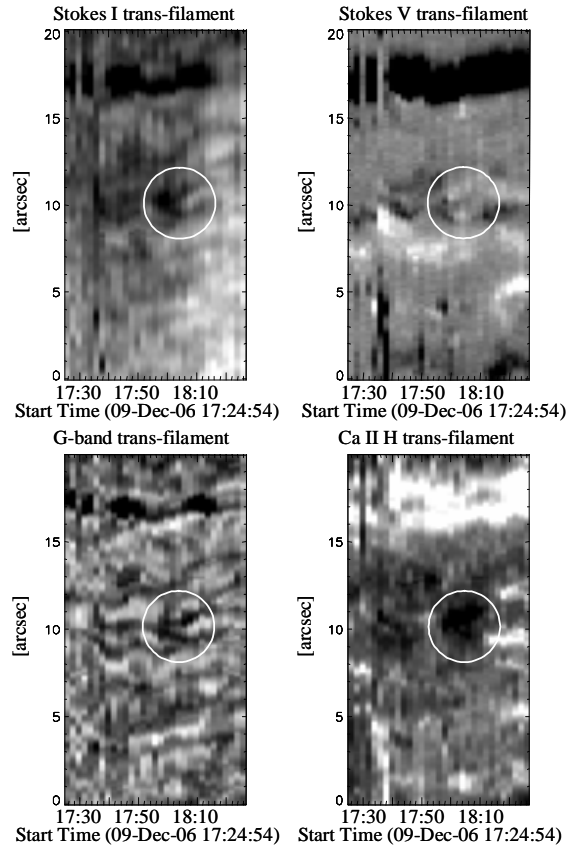
44

Figure 7: Trans-filament time-sliced diagram of the emerging flux. Upper left: Stokes I, upper right: Stokes V, lower left: G-band, lower right: Ca II H. Circles indicate the location of flux tube expansion.
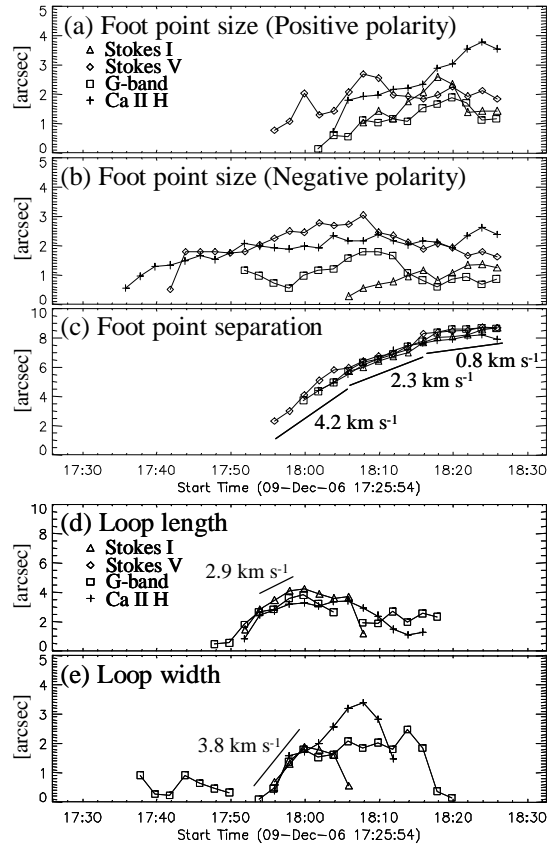
Figure 8: Temporal evolutions of measured quantities derived from time-sliced diagrams. (a) Footpoint size of positive polarities. (b) Footpoint size of negative polarities. (c) Footpoint separation. (d) Loop length. (e) Loop width.
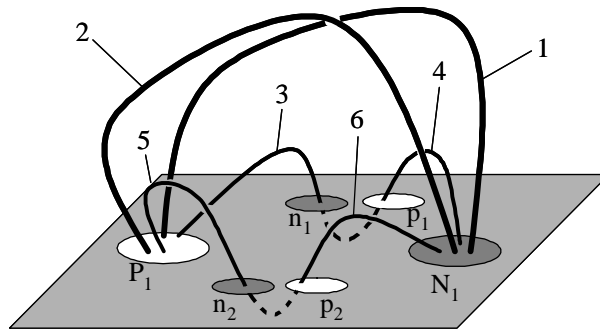

Figure 9: A model of the EFR. White and dark ovals represent the footpoints observed with Stokes V. Solid lines stand for magnetic tubes above the photosphere and dashed lines for those blow the photosphere. The numbers and alphabets in the figure correspond to the flux tubes and the footpoints in Fig. 5.

Part III

Observational Study of Eruptive Filament Using Solar Magnetic Activity Research Telescope

Abstract

We observed a filament eruption on solar limb by Solar Magnetic Research Telescope (SMART) in Hida observatory. Applying Beckers' cloud model to the data, we obtain Doppler velocity and optical depth distribution of the erupting filament. We also derived the transversal velocity so that we can calculate the 3D velocity distribution in the filament. From the optical depth of the erupting filament, we estimated the column mass and total mass of the filament. We discuss about the kinetic energy of the erupting filament.

1 Introduction

There are many previous studies about eruptive filaments. Sakurai (1975) categorized the evolution of a filament eruption into four phases: i) activation phase: filament is not so bright and rise slowly ($\sim$10 km s^{-1}). ii) Rapid rising phase: With sudden brightening the filament rises at higher speed (50$\sim$70 km s^{-1}). iii)Turbulent phase: The filament slow down and become turbulent. Sustained matter in the filament begins to fall down. iv) Remnant loop system phase: After almost all the matter has fallen down, there remains a thin loop-like system gradually fading away. Engvold et al. (1976) observed an eruptive filament with filtergraph and spectrograph and derived the three dimensional velocity to be 50$\sim$230 km s^{-1} for transversal motion and $-110 \sim +60$ km s^{-1} for line of sight motion. Kurokawa et al. (1987) observed a rotating eruption of a filament with Domeless Solar Telescope at Hida observatory.

2 Derivation of physical parameter in a filament

Beckers (1964) invented a new method to derive physical parameters of "cloud-like" structure on the solar surface. This method, therefore, was called "cloud model". With the cloud model, the contrast $C(\Delta\lambda)$ is described:

$$C(\Delta\lambda) \equiv \frac{I(\Delta\lambda) - I_0(\Delta\lambda)}{I_0(\Delta\lambda)} = \left[\frac{S}{I_0(\Delta\lambda)} - 1\right]\left\{1 - \exp\left[-\tau_0\exp\left(-\left(\frac{\Delta\lambda - \Delta\lambda_{\mathrm{I}}}{\Delta\lambda_{\mathrm{D}}}\right)^2\right)\right]\right\}.$$
(1)

where $I(\Delta\lambda)$ and $I_0(\Delta\lambda)$ are observed intensity and the reference profile emitted by the background, respectively. S, τ_0, $\Delta\lambda_{\mathrm{D}}$ and $\Delta\lambda_{\mathrm{I}}$ are the Hα source function, the optical

depth at line center, the Doppler width and the Doppler shift, respectively. Tsiropoula and Schmieder (1997) provided the way to derive the number density of hydrogen N_H from the optical depth τ_0. Assuming that τ_0 is written: $\tau_0 = \kappa_0 d$ where κ_0 is the line absorption coefficient and d is the path length along the line of sight through the filament. This formula can be written:

$$\tau_0 = \frac{\pi^{\frac{1}{2}} \mathrm{e}^2}{m_\mathrm{e} c} \frac{f \lambda^2}{c} \frac{N_2}{\Delta \lambda_\mathrm{D}} d \tag{2}$$

where $f = 0.641$ is the oscillator strength for Hα, m_e is the electron mass and N_2 is the number density of hydrogen atoms in the second quantum level. From this formula N_2 is derived as:

$$N_2 = 7.26 \times 10^7 \frac{\tau_0 \Delta \lambda_\mathrm{D}}{d} \quad [\mathrm{cm}^{-3}]. \tag{3}$$

Yakovkin and Zel'dina (1975) suggested the following relation:

$$N_\mathrm{e} = 3.2 \times 10^8 \sqrt{N_2} \quad [\mathrm{cm}^{-3}]. \tag{4}$$

Following the description in the Tsiropoula and Schmieder (1997), we can estimate the relation between N_H and N_2 to be:

$$N_\mathrm{H} = 5 \times 10^8 \times 10^{0.5 \log N_2} \quad [\mathrm{cm}^{-3}]. \tag{5}$$

From these values we calculate the total column mass M as:

$$M = (N_\mathrm{H} m_\mathrm{H} + 0.0851 N_\mathrm{H} \times 3.97 m_\mathrm{H}) d \tag{6}$$

where m_H is the mass of the hydrogen atom. 0.0851 and 3.97 mean the abundance ratio and weight ratio of helium to hydrogen, respectively.

3 Observation

The observation was performed on August 4, 2006 with Solar Magnetic Activity Research Telescope (SMART) at Hida observatory. The data were taken through the Lyot filter of SMART T1 with the wavelengths of Hα center, ± 0.5Å, ± 0.8Å. The observation cadence was 2 minutes. The pixel size is $0.5''$/pixel and the spatial resolution is about $2''$. The filament eruption started at 01:27 UT and ended 01:59 UT.

4 Result

From the transversal time-sliced diagram (Fig 2a), we obtain the erupting speed to be 40 km/s for the first few minutes and then accelerated up to 70 km/s. The matter in the filament fall at the speed of 45km/s. From the Doppler shift distribution (Fig. 2b and 2c) we estimate the angular velocity to be 7.9×10^{-3} rad/s. Fig 2d shows the distribution of the column density. d is assumed to be $25''$ from FWHM of the Hα intensity distribution. From these results the rotation and eruption energy of the filament are estimated to be 6.7×10^{27} erg for Rotation energy and 3.8×10^{28} erg for Eruption energy. For the future work, the time evolution of the energy of eruptive filaments will be studied.
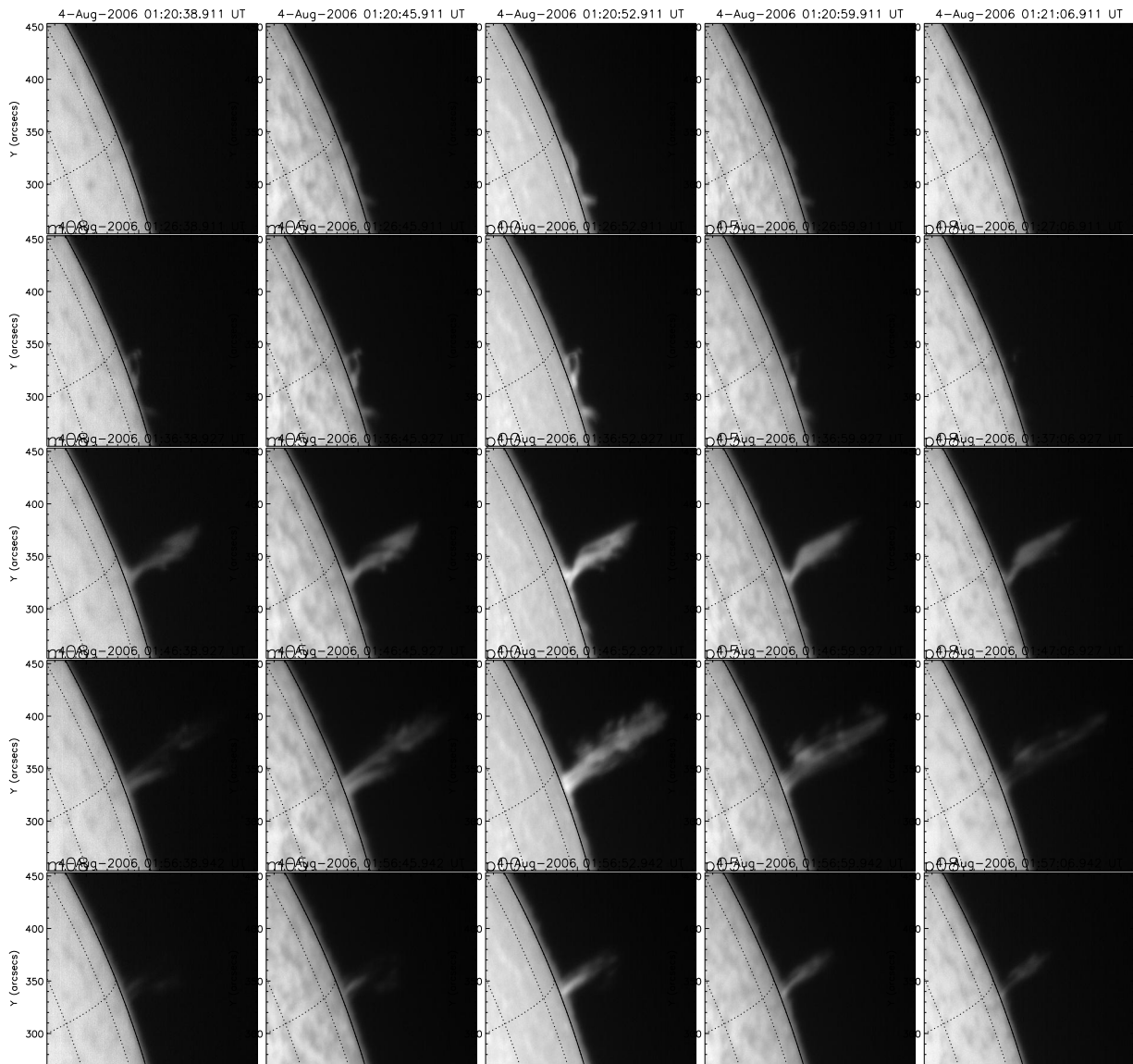
Figure 1: The observation result showing the evolution of the eruptive filament. The FOV is $200'' \times 200''$. The wavelength is Hα-0.8Å,-0.5Å,+0.0Å,+0.5Å and+0.8Å for each column. The observation time is 01:21 UT, 01:27 UT, 01:37UT, 01:47 UT and 01:57 UT for each row.
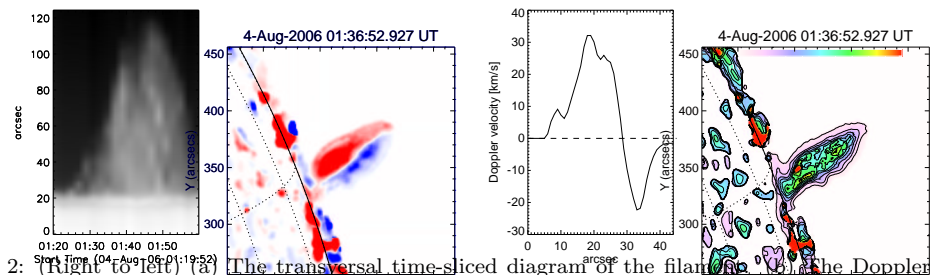

Figure 2: (Right to left) (a) The transversal time-sliced diagram of the filament. (b) The Doppler shift distribution of the filament. Plotting $-0.5 \sim +0.5$ Å. (c) The Doppler velocity along the dashed line in figure 2a. (d) The distribution of column density [g cm^{-2}].

References

Beckers, J. M. 1964, Ph. D. Thesis, Utrecht

49

Engvold, O., Rustad, B. M., & Malville, J. M. 1976, Sol. Phys., 48, 137

Kurokawa, H., Hanaoka, Y., Shibata, K., & Uchida, Y. 1987, Sol. Phys., 108, 251

Sakurai, T. 1976, PASJ, 28, 177

Tsiropoula, G., & Schmieder, B. 1997, A&A1, 324, 1183

Yakovkin, N. A., & Zel'dina, M. Yu. 1975, Sol. Phys., 45, 319